NanoSIMS results from olivine-hosted melt embayments: Magma ascent rate during explosive basaltic eruptions

Alexander S. Lloyd [a,*], Philipp Ruprecht [a,1], Erik H. Hauri [b,2], William Rose [c,3], Helge M. Gonnermann [d,4], Terry Plank [a,5]

[a] Lamont Doherty Earth Observatory, Columbia Univ., NY, USA
[b] Carnegie Instit. of Washington, DC, USA
[c] Michigan Tech Univ., Houghton, MI, USA
[d] Rice Univ., Houston, TX, USA

ABSTRACT

The explosivity of volcanic eruptions is governed in part by the rate at which magma ascends and degasses. Because the time scales of eruptive processes can be exceptionally fast relative to standard geochronometers, magma ascent rate remains difficult to quantify. Here we use as a chronometer concentration gradients of volatile species along open melt embayments within olivine crystals. Continuous degassing of the external melt during magma ascent results in diffusion of volatile species from embayment interiors to the bubble located at their outlets. The novel aspect of this study is the measurement of concentration gradients in five volatile elements (CO_2, H_2O, S, Cl, F) at fine-scale (5–10 μm) using the NanoSIMS. The wide range in diffusivity and solubility of these different volatiles provides multiple constraints on ascent timescales over a range of depths. We focus on four 100–200 μm, olivine-hosted embayments erupted on October 17, 1974 during the sub-Plinian eruption of Volcán de Fuego. H_2O, CO_2, and S all decrease toward the embayment outlet bubble, while F and Cl increase or remain roughly constant. Compared to an extensive melt inclusion suite from the same day of the eruption, the embayments have lost both H_2O and CO_2 throughout the entire length of the embayment. We fit the profiles with a 1-D numerical diffusion model that allows varying diffusivities and external melt concentrations as a function of pressure. Assuming a constant decompression rate from the magma storage region at approximately 220 MPa to the surface, H_2O, CO_2 and S profiles for all embayments can be fit with a relatively narrow range in decompression rates of 0.3–0.5 MPa/s, equivalent to 11–17 m/s ascent velocity and an 8 to 12 minute duration of magma ascent from ~10 km depth. A two stage decompression model takes advantage of the different depth ranges over which CO_2 and H_2O degas, and produces good fits given an initial stage of slow decompression (0.05–0.3 MPa/s) at high pressure (>145 MPa), with similar decompression rates to the single-stage model for the shallower stage. The magma ascent rates reported here are among the first for explosive basaltic eruptions and demonstrate the potential of the embayment method for quantifying magmatic timescales associated with eruptions of different vigor.

© 2014 Elsevier B.V. All rights reserved.

1. Introduction

A critical parameter governing the style and intensity of volcanic eruptions is the rate at which magma ascends from the storage region to the surface. The decompression of ascending magma drives the exsolution of dissolved volatile components from the melt into a separate vapor phase, which increases the buoyancy of the magma and creates a driving force for further ascent and eruption. The interaction of the rate of ascent with the kinetics of bubble nucleation, growth, and coalescence is also an important factor controlling the development of permeability in magmas and therefore how magmas degas and ultimately erupt (Gonnermann & Manga, 2007; Cashman and Sparks, 2013). Although several factors and feedbacks may affect the style in which magmas erupt, magma ascent rate is fundamental to the dynamics of eruption. However, it is a parameter that has proved difficult to determine, with current estimates limited to a few well-documented eruptions (Rutherford, 2008).

* Corresponding author at: Lamont Doherty Earth Observatory, 127 Comer, 61 Route 9W - PO Box 1000, Palisades, NY, 10964-8000, USA. Tel.: +1 845 365 8926; fax: +1 845 365 8155.
E-mail addresses: alloyd@ldeo.columbia.edu (A.S. Lloyd), ruprecht@ldeo.columbia.edu (P. Ruprecht), hauri@ciw.edu (E.H. Hauri), raman@mtu.edu (W. Rose), helge@rice.edu (H.M. Gonnermann), tplank@ldeo.columbia.edu (T. Plank).
[1] Tel.: +1 845 365 8635.
[2] Tel.: +1 202 478 8471.
[3] Tel.: +1 906 487 2367.
[4] Tel.: +1 713 348 6263.
[5] Tel.: +1 845 365 8410.

Many approaches have been employed to quantify magma ascent rates, including but not limited to: fluid dynamical simulations, seismicity, decompression crystallization and bubble nucleation experiments, crystal reaction kinetics, elemental diffusion during ascent, or a combination of these techniques (e.g. Spera, 1984; Endo et al., 1996; Geschwind and Rutherford, 1995; Rutherford and Devine, 2003; Proussevitch and Sahagian, 2005; Szramek et al., 2006; Toramaru, 2006; Castro and Dingwell, 2009; Ruprecht and Plank, 2013). These approaches have revealed magma ascent rates that vary over orders of magnitude (0.1–30 m/s) for volcanism with a diversity of magma composition and viscosity, eruption explosivity, and depth resolution from source to vent (i.e. some techniques are sensitive in the shallow crust, while others may provide deeper constraints). Here, we pursue an approach, in which we make use of the preservation of chemical zonation in crystals or glass, and then apply time-dependent diffusion models to obtain the duration of magma ascent (e.g., Demouchy et al., 2006; Peslier and Luhr, 2006; Liu et al., 2007; Ruprecht and Plank, 2013). Our study focuses on hydrous mafic arc volcanism, for which few previous estimates of ascent rate exist.

A petrologic approach that holds much promise for constraining ascent timescales involves the analysis of chemical zonation of volatile species in melt embayments that are found within phenocryst phases (Anderson, 1991; Liu et al., 2007; Humphreys et al., 2008). Essentially melt inclusions (MIs) that have failed to become fully enclosed, melt embayments have also been termed hourglass inclusions, melt pockets, melt tubes, and re-entrants. With the exception of hourglass inclusions that are connected to the exterior melt via a very narrow neck of glass (Anderson, 1991), all of these other features refer to some crystal growth defect that fills with melt and remains connected to the external melt through a wide outlet on the crystal face. While most fully-enclosed melt inclusions preserve magma compositions prior to degassing (Metrich and Wallace, 2008), embayments inevitably experience diffusive volatile loss due to the direct connection to the host melt during ascent and degassing. In some cases this volatile loss is only partial and compositional gradients within the embayment may constrain the timescales of diffusive re-equilibration, which can be related to the decompression rate.

The key assumptions in this approach are that the chemical species of interest within the embayment attempt to remain in equilibrium with an external melt undergoing equilibrium degassing and that the resultant diffusion profile can be spatially resolved to extract meaningful time scales. As near-surface magma ascent is rapid for explosive eruptions, only fast-diffusing volatiles, such as H_2O, CO_2 and S, capture the ascent process. In a pioneering study, Liu et al. (2007) measured H_2O and CO_2 by FTIR in quartz-hosted embayments. However, the large FTIR beam size limited the analysis to two to three spots, and such coarse spatial resolution compromises the temporal resolution. Humphreys et al. (2008) later utilized the embayment technique with plagioclase-hosted embayments, correlating H_2O concentration with gray scale values measured by electron back-scatter (EBS) for a highly spatially resolved profile. Although they achieved better spatial resolution especially in the critical region near the outlet, the EBS method is unable to quantify the additional constraint on ascent and pressure provided by CO_2.

Here we attempt to improve upon prior work by utilizing the unique analytical capabilities of the NanoSIMS (Hauri et al., 2011), which allows for a spatial resolution (<0.1 to 10 μm raster size) approaching that of the EBS technique, while enabling the analysis of multiple volatile species (H_2O, CO_2, S, Cl, F). We focus on the well-documented October 1974 eruption of Volcán de Fuego (Rose et al., 1978), which was meticulously sampled and includes a comprehensive melt inclusion record (Roggensack, 2001; Berlo et al., 2012; Lloyd et al., 2013). In this study, we model the diffusion of multiple volatile species within melt embayments in olivine to determine magma decompression rate and its relationship to volcanic explosivity.

2. Background

This study utilizes the same airfall samples of the Volcán de Fuego October 1974 eruption as in our previous study on melt inclusions (MIs) and the timescales of volatile loss (Lloyd et al., 2013). Four sub-Plinian eruptions (VEI 4) occurred between October 14 and October 23, 1974, producing ~0.1 km^3 of porphyritic, H_2O-rich, high-aluminum basalt (Rose et al., 2008). A comprehensive sample suite was collected by S. Bonis during each eruptive phase. Here we focus on samples erupted on October 17, 1974, to ensure that the analyzed embayments underwent similar ascent, eruptive, and depositional histories, and not the shifts in eruptive behavior often observed during multi-day eruptions (e.g. 2010 Eyjafjallajokull, Gudmundsson et al., 2012). The October 17 phase of the eruption was the most explosive of the 4 main phases and produced about 40% of the total erupted material (Rose et al., 1978). Furthermore, this phase exhibited a sustained eruptive sequence that does not include the complexities associated with the initiation or cessation of the eruption (Carr and Walker, 1987).

The October 17 phase has been described as a sub-Plinian eruption with major ash flows and extensive airfall from an eruption column that reached stratospheric heights (~15 km, Rose et al., 1978). Intense explosions with a one-minute periodicity were observed near the vent. The pulsating explosions and bimodal grain size distribution of the tephra suggest that a comminution or milling process could be occurring post-fragmentation in the upper conduit and vent during the eruption (Rose et al., 2008). After the 1974 eruption, the main surface vent of Fuego was observed to be greater than 20 m in radius and was hypothesized to be connected to the source region by a vertical conduit (Rose et al., 1978).

The extensive prior work on MIs from the October 17 phase of the eruption provides a useful starting point for understanding the pre-eruptive conditions and decompression path during magma ascent. Shifts in bulk ash geochemistry (Rose et al., 1978), changes in the size and modal proportions of phenocrysts (Roggensack, 2001), and MI heterogeneity (Berlo et al., 2012) have all been presented as evidence for the hybridization of distinct magmas during this 10-day long eruption. It has been speculated that the 1974 eruption either tapped a vertically stratified magma chamber (Rose et al., 1978), or that magma ascent was preceded by mixing of magmas, which fractionated at different depths (Roggensack, 2001; Berlo et al., 2012).

Our work on Fuego MIs erupted on October 17 indicates that a simpler magma system was associated with this phase of the eruption. The linear variation in K_2O–SiO_2, as well as consistent trace-element ratios, reflect degassing-induced crystallization of a single parental magma (Lloyd et al., 2013). This could reflect a fresh influx of basaltic melt preceding the explosive October 17 eruption, whereas the other, less explosive eruptions may have included residual magma that stalled within the plumbing system (Berlo et al., 2012). In Lloyd et al. (2013), we analyzed MIs from multiple pyroclasts of different sizes (ash, lapilli, and volcanic bombs) and discovered systematically lower (~1 wt.%) H_2O concentrations in MIs from both the core and the rim of two 6 cm bombs, compared to those in ash and lapilli samples. We interpreted this to reflect diffusive H_2O-loss through the olivine host during post-eruptive cooling, on a timescale of approximately 10 min. However, because H_2O-loss from ash and lapilli hosted MIs could not be accounted for by post-eruption cooling alone, we considered the possibility that some H_2O-loss also occurred during ascent, and estimated magma ascent rates on the order of 10 m/s. Once the MIs were corrected for post-entrapment diffusive re-equilibration, the volatile concentrations conformed to a closed-system degassing path, indicating that the MIs were trapped at various depths prior to and during ascent. Here, we use this closed-system degassing path and the associated range of MI entrapment pressures to define initial and external boundary conditions for embayment formation and ascent. By exploiting the differences in solubility and diffusivity of five volatile species, this embayment study provides independent constraints on

ascent rates that can be compared to the previous estimate derived from olivine-hosted MIs.

3. Methods

3.1. Sample preparation

During sample preparation, special care was taken to consider the size of each pyroclast and the effect on post-eruptive cooling. Samples were divided into three sizes: volcanic ash (particles with a diameter <2 mm); lapilli (diameter between 2 mm and 64 mm); and volcanic bombs (clasts with a diameter >64 mm). The ash sample (VF-132 - IGSN: ASL000001) was sieved without crushing, and loose olivine grains were selected from 250-500 μm and from 500-1000 μm size fractions. The lapilli sample (VF-129 - IGSN: ASL000002) was collected as a mix of ash and lapilli ranging in size from 30 mm to less than 0.1 mm. Only pyroclasts greater than 20 mm in diameter were selected; and of this set, the five largest lapilli were chosen. The bomb sample (VF-137B - IGSN: ASL000003) was selected from a diverse collection for its uniform spherical shape and relatively large size (60-mm diameter). The bomb was cut so that the material sampled for olivine-hosted embayments was derived from the inner $20 \times 20 \times 20$ mm^3 of the bomb. The vesiculation in these pyroclasts was relatively uniform between clast types and ranged from 40% to 55% (estimated by bubble size distribution techniques, Gray A.L., pers comm, 2012); groundmass color was observed to be consistent among all the samples.

After crushing, olivine phenocrysts and fragments (~10% by volume) were separated by hand from groundmass (~60%), plagioclase (~25%), opaque minerals (3%), and clinopyroxene (~2%). Phenocrysts were then picked for optimal melt embayments within the olivine. Although MIs with ideal characteristics are relatively common in these samples, embayments are extremely rare and special care is needed during preparation. In order to approximate one-dimensional diffusion, we selected glassy embayments with a simple tubular shape that were free of secondary inclusions. We chose embayments with evidence of a single bubble at the outlet, ensuring a path to vapor and communication with the conditions in the exterior melt during decompression. Phenocrysts were mounted individually in dental resin and polished on one side parallel to the long axis of the embayment to expose the maximum cross-sectional area for analysis. Once the embayments were exposed, the phenocrysts were removed from the resin and mounted together in indium metal for NanoSIMS (Secondary Ion Mass Spectrometer) and EMP (Electron Micro Probe) analysis. Analysis of the embayments by NanoSIMS was completed first, in order to avoid potential H$_2$O-loss during exposure to the electron beam and the possibility of CO$_2$ contamination by the EMP carbon coat. Back-scattered electron images were taken for each inclusion after the NanoSIMS analysis.

3.2. Ion microprobe analysis

Volatiles (H$_2$O, CO$_2$, Cl, F, and S) in the embayments were measured in one session on a Cameca NanoSIMS 50L at the Carnegie Institute of Washington (CIW), Department of Terrestrial Magnetism. The procedures followed those in Hauri et al. (2011); each location was pre-sputtered for 60 s using a 10 μm × 10 μm raster to remove surface contaminants. After the presputter, the raster size was reduced to 7.5 μm × 7.5 μm, with electronic gating (beam blanking) used to discard data from the crater edge, such that the reported data represent an area within the sputter crater measuring 2.5 μm × 2.5 μm. Six replicate analyses of a basaltic glass secondary standard (GL07 D30-1, Hauri et al., 2006) yielded 2 relative standard deviations (standard deviation/average; RSDs) of 4.8% for ^{12}C, 5.8% for ^{16}O^{1}H, 6.6% for S, 8.0% for F, and 7.6% for Cl (see Supplementary Table 1 for calibration standards).

3.3. Electron microprobe analyses

Embayments and olivine phenocrysts were analyzed for major elements using a Cameca SX100 microprobe (EMP) at the American Museum of Natural History (AMNH). The analyses of the embayments were performed parallel to the direction of NanoSIMS analysis (Fig. 1). The host olivine phenocryst was then analyzed within 20 μm from the inner border with the embayment. Major elements in hydrous glasses and olivine phenocrysts were analyzed using a 10 nA beam current (4-nA for Na; 40-nA for Cl and S) and a 15 kV accelerating potential with a 5 μm diameter beam. Count times on peak for major elements varied between 20s (Na, Mg, Si, K), 30s (Ca, Mn, Al, Fe), 40s (Ti and P), 60s (Cl), and 80s (S). Background count times for the elements were 50% of their peak counting times. Replicate analysis of two basaltic glass check standards (FR:ND-60-01 (5), MR:ND-70-01 (5)) yielded average 2 RSDs of less than 4% for major elements SiO$_2$, Al$_2$O$_3$, FeO, MgO, and CaO. Average 2 RSDs for K$_2$O, TiO$_2$, Na$_2$O, S, and Cl were in the 10%–15% range while MnO and P$_2$O$_5$ were ~25%. Sulfur and chlorine are within 22% and 14% of the NanoSIMS measurements, respectively. Because we later model the S profile in detail, we note that the electron probe and NanoSIMS profiles largely overlap, after adjustment for the 15–20% offsets (see Supplementary Table 2). We use the NanoSIMS data below in all figures and calculations, because the precision is better, and all volatiles are measured in the same spots.

4. Results

4.1. Melt embayment morphology

We report analyses of four olivine-hosted melt embayments from the October 17, 1974 Fuego eruption: two from the ash sample (VF-132), one from lapilli (VF-129), and one from the small bomb (VF-137B). The sample names for each embayment have been shortened and are represented in the following way, in ascending order of length: E1 (VF-129-E2), E2 (VF-132-E1), E3 (VF-132-E4), and E4 (VF-137B-E1). The four embayments display a range in size (100–200 μm) and shape (Fig. 1), but all exhibit well-quenched glass with no evidence of co-entrapped phases or daughter crystals. Although not all of the embayments terminate on polyhedral crystal faces (Fig. 1), all exhibit evidence of matrix glass adjacent to the outlet bubble, indicating that the embayment was communicating with the surrounding melt. Additionally, all reported embayments were straight enough to justify one-dimensional diffusion modeling. The rounded edges of the embayment interiors suggest that they were formed through some slow-growth mechanism and are not remnants of healed grain boundaries (Faure and Schiano, 2005). The most important characteristic shared among all four embayments is a bubble at the outlet of the tube (Fig. 1).

Some distinctions need to be made in the terminology for the distances reported. The outlet refers to the gap in the host olivine where the contents (melt or gas) of the embayment interact with the surrounding magma. The distance to the bubble is the distance from an analysis point to the termination of the glass (start of the bubble) and does not take into account the embayment outlet. Although three of the embayments were straightforward to interpret in this way, E1 presented challenges because it was not polished at the maximum cross section of the bubble. A transmitted-light photomicrograph of the embayment (Supplementary Table 3) was used to measure the distance to the bubble in three dimensional space, which resulted in a shift of 7 μm from the distances apparent in Fig. 1.

As the exterior and interior melt degas during decompression, the outlet bubbles are potentially undergoing dynamic changes in their size and shape that may limit the amount of glass that remains in the embayment. Although the distance from the terminus of the glass in the embayment to the outlet (i.e. the size of the bubble) varies, we assume that the melt in the embayment is in the process of re-equilibrating with the decompressing bubble and that the distance to the outlet from the
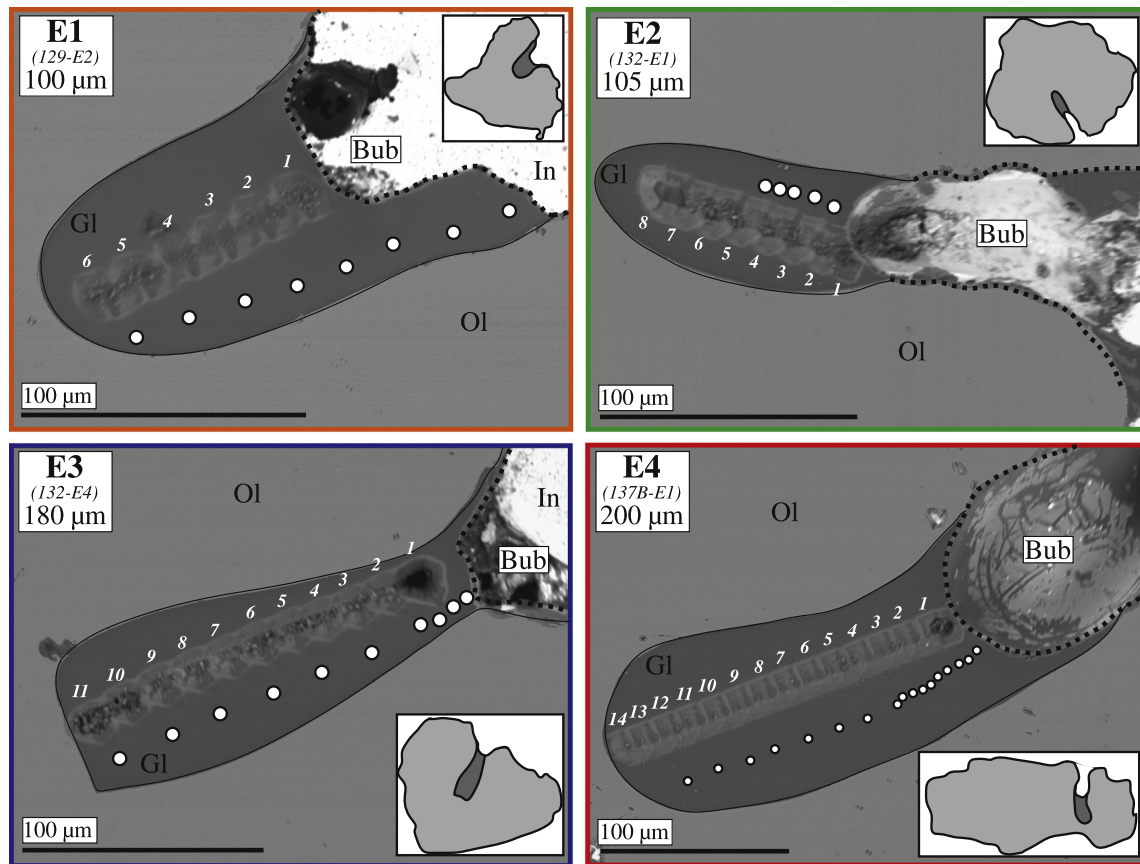
Fig. 1. Electron back-scatter images of the four embayments studied here, and locations of the analysis spots. NanoSIMS measurement locations can be seen as small, numbered craters in the dark gray glass (Gl) (distances reported in Table 2). EMP measurements are represented by white circles (distances reported in Supplementary Table 4). The host olivine is light gray (Ol); the void spaces are interpreted to be evidence for a bubble (Bub), and the highly reflective areas are the indium metal (In) mounting medium. The total length of the glass in each embayment is reported in μm under the sample ID. Brightness was altered to increase the contrast between the embayment glass (outlined in black for clarity) and host olivine. The inset sketches show the size and location of the embayment relative to the host phenocryst.

terminus of the glass is not relevant for modeling the decompression rate. Changes in bubble size could lead to a moving boundary problem. However, the relative incompressibility of the internal melt in comparison to the ability of the bubble to freely expand into the surrounding matrix may reduce this possibility. For simplicity and the lack of evidence for a moving or deforming boundary, we assume that the initial volume of melt in the embayment is conserved throughout decompression.

4.2. Major element variations in embayments

The olivines that host the studied embayments have forsterite contents (72–75) that are similar to those measured previously from this day of the eruption (72–78; Lloyd et al., 2013). Assuming an $Fe^{3+}/\Sigma Fe$ ratio of 0.20 and a $K_D = 0.35$ (as in Lloyd et al., 2013), the highest Mg# measured in the glass for each embayment is in equilibrium with the host olivine, except for E1, which may have experienced ~5% of

post-entrapment crystallization, presumably at the interface between melt and host olivine. Because we are primarily concerned with volatile species in the melt embayment, no corrections to the major-element concentrations were applied for this crystallization.

The concentration of major elements in the inner regions of the embayments is uniform (within the error of the EMP measurements), and falls within one standard deviation of previous measurements in MIs for this day of the eruption (Table 1; Lloyd et al., 2013). TiO_2 and CaO (and to a lesser extent Al_2O_3) are exceptions, with concentrations consistently higher than what is measured in the MIs. Similar to previous studies, the measured compositions classify the Fuego melts as a high-alumina basaltic andesite.

In the 20–40 μm approaching the exit bubble, all embayments show concentration gradients (illustrated in Fig. 2 for E4, but also present for all embayments; see Supplementary Table 4 for all EMP analyses). The length of this chemical boundary layer varies among the four

Table 1
The major-element concentrations measured in the embayment glass (excluding the outer boundary layer as in Fig. 2) compared to the average MI erupted on the same day of the 1974 eruption (from Lloyd et al., 2013). The embayment concentrations are uncorrected and the MI compositions were corrected with the standard PEC correction techniques (see Lloyd et al., 2013).

Sample distance		SiO_2	TiO_2	Al_2O_3	FeO^T	MnO	MgO	CaO	Na_2O	K_2O	P_2O_5	Total
Average MI (1 SD)		52.07 (2.51)	1.06 (0.13)	17.10 (0.89)	9.28 (0.73)	0.15 (0.03)	4.16 (0.46)	7.47 (0.96)	3.70 (0.41)	0.86 (0.18)	0.25 (0.05)	96.29 (1.03)
El-7	60	51.97	1.23	17.97	9.99	0.20	3.69	8.71	3.74	0.87	0.20	99.00
E2-5	28	52.73	1.27	18.21	9.99	0.16	3.56	8.79	4.03	1.04	0.21	100.44
E3-8	115	51.94	1.20	17.74	9.76	0.18	4.09	8.62	3.70	0.81	0.21	98.70
E4-15	127	50.90	1.22	17.80	10.02	0.19	4.23	8.63	3.96	0.81	0.19	98.39
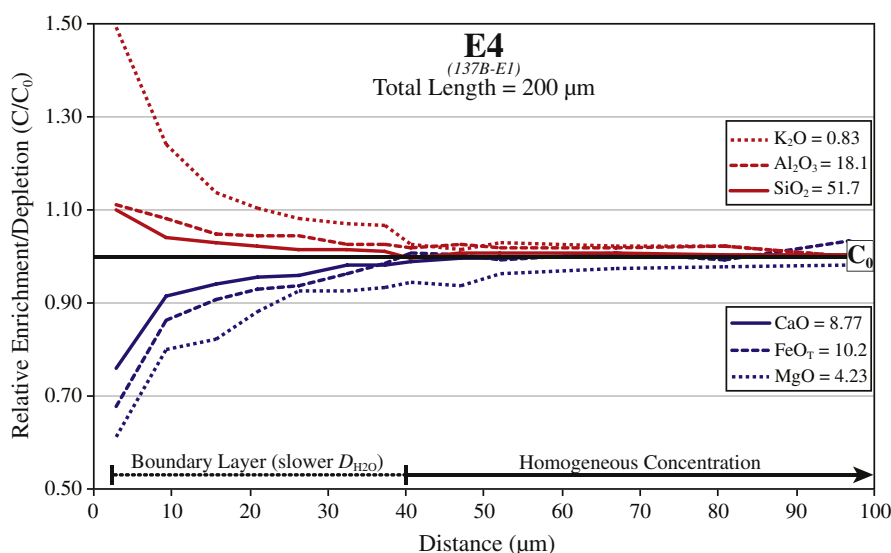
Fig. 2. Major-element concentration gradients in glass near the contact between the melt and bubble for embayment E4. Distance is reported in μm from the bubble inwards to the embayment interior. Relative enrichment (red elements) or depletion (blue elements) was calculated by dividing the measured concentration by the initial concentrations (C_0), taken from the regions of homogeneous concentration in the interior of the embayment (C_0 reported as wt.% in the figure key). The boundary layer is consistent with crystallization of olivine and clinopyroxene on the bubble wall, and the compositional changes are taken into account when calculating the diffusivity of water (D_{H_2O}). (For interpretation of the references to color in this figure legend, the reader is referred to the web version of this article.)

embayments and differs in shape depending upon the element in question. The magnitude of enrichment or depletion in this boundary layer appears to be dependent on the compatibility of the element (i.e., greatest enrichment for the most incompatible element, K_2O, and greatest depletion for most compatible, MgO). On the other hand, the length of the boundary layer decreases in the order K_2O, CaO, FeO, MgO, Al_2O_3, and SiO_2 (from 40 to 20 μm respectively; Fig. 2), which is in agreement with the elements' respective rates of diffusion in mafic melt (Zhang et al., 2010). The components MgO, FeO, and CaO behave compatibly and decrease in concentration toward the bubble; whereas, SiO_2, Al_2O_3, and K_2O increase toward the bubble (Fig. 2). These patterns are consistent with the crystallization of primarily olivine as well as clinopyroxene but not plagioclase, which is the most abundant phase in the eruptive products (perhaps reflecting an inability of plagioclase to nucleate on the bubble wall in the embayment). Observed under transmitted or reflected light (Fig. 1 and Supplementary Table 3), there is no observable crystallization within the vitrified embayment glass or on the bubble/glass interface. Mass-balance calculations of the observed decrease in MgO, FeO, and CaO indicate that any potential crystal growth would be less than 2 μm in thickness, so any visible evidence for crystallization may be difficult to resolve with optical microscopy. It should be noted that this compositional boundary layer observed in the Fuego embayments precludes the use of the back-scattered electron (BSE) method used in Humphreys et al. (2008) to estimate H_2O concentration, because the major-element variations dominate over the H_2O variations in controlling BSE gray scale intensity.
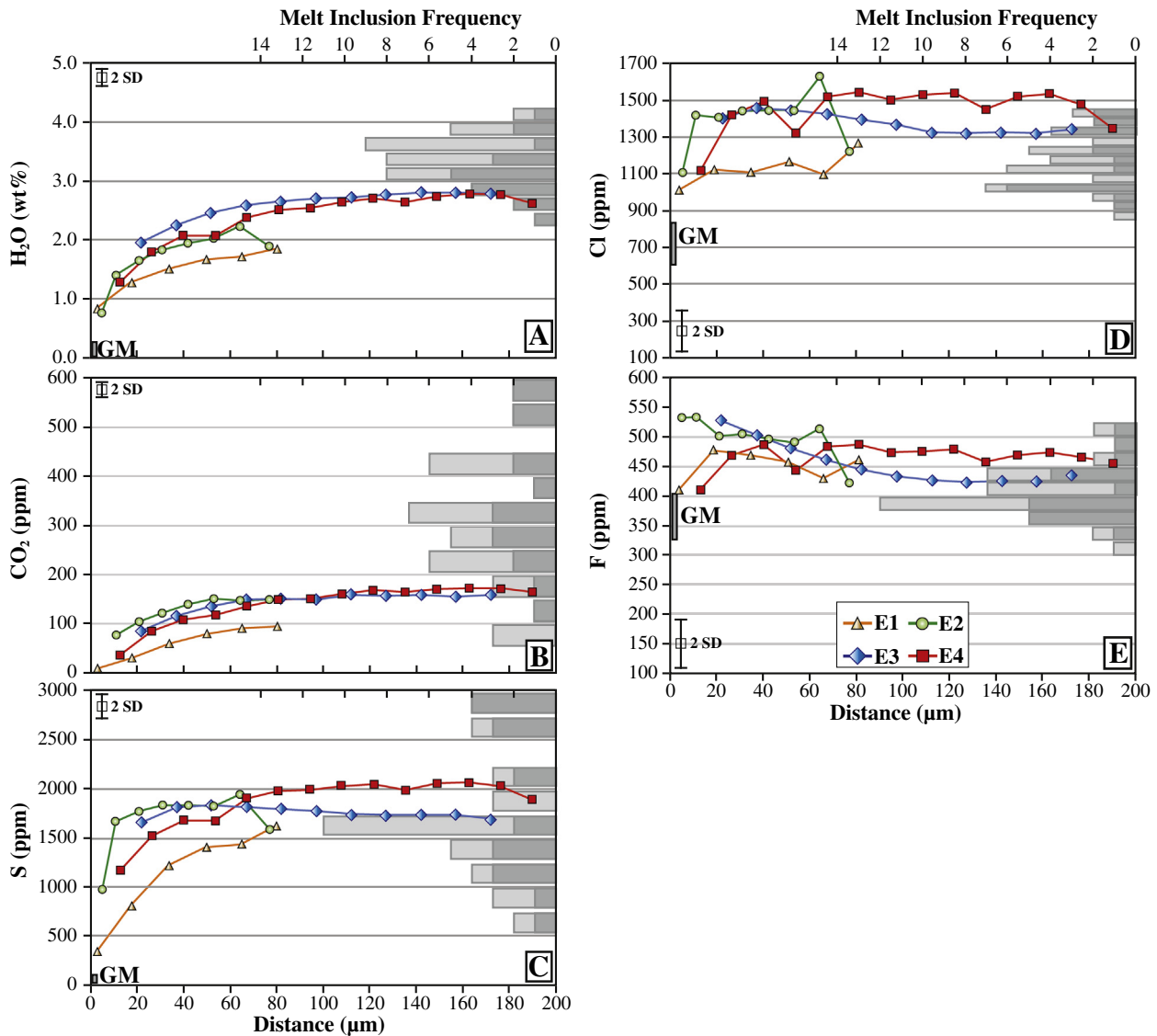
4.3. Volatile concentrations in embayments

In all four embayments, CO_2, H_2O, and S decrease in concentration toward the outlet bubble, whereas Cl and F vary little throughout the embayments (Fig. 3; Table 2). The concentrations in these embayments differ considerably from fully-enclosed melt inclusions, most notably H_2O (Fig. 3A). For example, H_2O concentrations in the embayments are uniformly <3 wt.%, while those in the melt inclusions from the ash and lapilli samples are uniformly >3 wt.%. The only MIs that overlap in H_2O with the embayments originate from more slowly cooled bomb samples (indicated by dark gray in Fig. 3) that appear to have lost H_2O by diffusion through their host olivine (Lloyd et al., 2013). The two longest

embayments (E3 and E4) have the highest H_2O concentrations, whereas the two shorter embayments (E2 and E1) have lower concentrations at similar distances from the bubble, consistent with diffusive H_2O-loss. All of the embayment concentrations, however, are greater than the highly degassed values measured in the groundmass glass (<0.06 wt.%; see Supplementary Table 5).

CO_2 also decreases toward the bubble (Fig. 3B), again, with the two longest embayments having higher maximum CO_2 concentrations than the shorter embayments. The CO_2 concentration gradient for E2 is shallower than in the other embayments (Fig. 3B). While the MIs have a narrow range in H_2O concentrations (3–4 wt.%), MI CO_2 concentrations vary over a much wider range (100–750 ppm). With fewer than 20% of the MI analyses overlapping with the maximum measured CO_2 in the embayments (Fig. 3B), it is unlikely that the interior of the embayments represents the initial concentration of CO_2. Previous work was unable to report CO_2 concentrations in the Fuego groundmass glass due to contamination (Lloyd et al., 2013), but they are likely to be lower than the lowest concentrations recorded in the embayments.

Sulfur also decreases toward the bubble, but unlike H_2O and CO_2, the S concentrations of the interior of all four embayments fall within the peak of the MI population (1250–2250 ppm, Fig. 3C). The embayment interiors thus appear to retain initial S concentrations that are unaffected by diffusive loss, consistent with the relative diffusivities of H_2O, CO_2, and S (Baker et al., 2005). Three embayments continually decrease in S, whereas E3 (and E2 to a lesser extent) shows a complex pattern of increasing and then decreasing S toward the exterior (Fig. 3C). The S concentrations in the groundmass glass are lower than the lowest recorded in the embayments.

The concentrations of Cl in the embayments largely overlap with those of the MI population, albeit occupying the enriched end of the MI spectrum. Moreover, throughout the length of the embayment, Cl remains relatively constant. This contrast in the behavior of Cl relative to H_2O, CO_2 and S may reflect its lack of partitioning into a vapor phase over much of the magma ascent path. Indeed, Cl varies inversely with H_2O and S in Fuego MIs, rising in concentration during degassing like a magmaphile element (Lloyd et al., 2013). Nonetheless, the Cl concentration in the Fuego groundmass glass is notably lower than the MIs or embayments, and likely reflects degassing of Cl at pressures lower than those recorded in the MIs (i.e., <150 MPa). Degassing may also be recorded in the analysis point closest to the embayment bubbles

Fig. 3. Volatile concentrations within melt embayments plotted as distance from the outlet bubble. Gray bars are histograms of the uncorrected melt inclusion data for the same day of the eruption (with dark gray representing MIs from the volcanic bomb-hosted melt inclusions and light gray from those hosted in ash and lapilli). Groundmass glass (GM) concentrations (Supplementary Table 5) are plotted at zero distance for reference.

(between 6 and 22 μm, Table 2), where Cl decreases abrupt-imately 100 ppm for E1 and E3, or 300 ppm for E2 and E4).

The concentration of F in the embayments also largely overlaps with that in the MIs, but it shows inconsistent behavior along the embayments (Fig. 3E). In two cases (E3, E2), F increases smoothly by a factor of ~1.2 from the embayment interior to the bubble. The two other embayments (E4, E1) show a relatively flat concentration profile with a drop in concentration of ~60 ppm at the analysis spot closest to the bubble. F is the most magmaphilic of the volatile elements, with no evidence for degassing. This is apparent in the overlap in F between the groundmass glass (350–400 ppm) and the peak in the MI population (Fig. 3E).

4.4. Coupled volatile-major element variations in embayments

Fig. 4 plots the volatile elements, H_2O, CO_2, S and Cl, vs. SiO_2 in the embayments and the fully enclosed MIs from Lloyd et al. (2013). The SiO_2 concentrations clump at low values in the uniform embayment interiors, and extend to high values within the 20–30 micron boundary layer near the bubble (i.e., as in Fig. 2). The embayment interiors plot at the low SiO_2 and high S end of the MI array, consistent with an initial composition that coincides with the most primitive for the eruption. Lloyd et al. (2013) interpreted the MI array to reflect coupled degassing and crystallization during ascent, to explain the increase in SiO_2 and decrease in S, for example. From this perspective, the embayments would reflect an origin early in the ascent history. Embayment interiors coincide with the MI array for S, but fall well below the array for H_2O and CO_2. All of the embayment interiors are enriched in Cl at the same SiO_2 as the MI, by up to 20–40%. All of these variations (except Cl) are consistent with loss of volatiles toward the vapor bubble, at the same time that crystallization around the bubble leads to an increase in SiO_2. The different trajectories of the MI array and the embayment profiles likely result from different processes: diffusive loss of volatiles from the open embayments vs. entrapment of degassing melt at variable depths for the MIs. In the next section, we use these inferences along with a numerical diffusion model to describe the embayment profiles for H_2O, CO_2 and S. There may be further information in the behavior of Cl and major elements, but these appear to be complicated by multi-phase crystallization and other less well understood processes.

Table 2

NanoSIMS results for the analyses shown in Fig. 1 (*nd*, not detected). Distance is measured from the outlet bubble. See Supplementary Table 1 for calibration standards and error calculation.

Analysis	Dist. (μm)	CO_2 (ppm)	H_2O (wt.%)	F (ppm)	S (ppm)	Cl (ppm)
E1-1	2	9	0.83	411	335	1011
E1-2	17	32	1.28	477	814	1124
E1-3	33	61	1.51	469	1224	1109
E1-4	49	79	1.67	458	1410	1164
E1-5	64	91	1.72	431	1439	1098
E1-6	79	96	1.85	461	1620	1265
E2-1	5	*nd*	0.76	532	982	1105
E2-2	11	78	1.42	534	1667	1419
E2-3	21	105	1.66	503	1777	1406
E2-4	31	123	1.83	504	1832	1442
E2-5	42	139	1.95	497	1838	1444
E2-6	53	151	2.02	491	1827	1444
E2-7	64	148	2.24	514	1945	1628
E2-8	77	150	1.89	422	1591	1220
E3-1	22	86	1.95	527	1659	1407
E3-2	37	116	2.26	504	1821	1457
E3-3	52	137	2.46	480	1835	1445
E3-4	67	149	2.59	462	1821	1424
E3-5	82	152	2.66	445	1793	1394
E3-6	97	150	2.70	434	1775	1366
E3-7	112	159	2.73	427	1746	1327
E3-8	127	158	2.78	424	1744	1323
E3-9	142	159	2.80	425	1742	1324
E3-10	157	155	2.81	425	1735	1321
E3-11	172	160	2.78	435	1704	1341
E4-1	13	37	1.28	411	1177	1120
E4-2	27	85	1.80	469	1528	1418
E4-3	40	108	2.07	487	1686	1492
E4-4	54	119	2.07	444	1679	1321
E4-5	67	136	2.38	484	1907	1517
E4-6	81	150	2.51	487	1982	1544
E4-7	95	152	2.54	475	1996	1506
E4-8	108	162	2.63	476	2035	1531
E4-9	122	168	2.71	478	2055	1542
E4-10	135	166	2.65	459	1991	1452
E4-11	149	171	2.74	469	2062	1521
E4-12	163	173	2.79	474	2073	1533
E4-13	176	173	2.76	466	2032	1476
E4-14	190	165	2.62	456	1892	1348

5. Discussion

5.1. Diffusion modeling

In order to use the volatile concentrations as chronometers for magma ascent, several parameters must be known in order to constrain the time during which diffusion took place: the initial conditions prior to decompression; the changing external melt during ascent, and the diffusivity of each volatile species. The concentration profiles are modeled using a one-dimensional diffusion model that evolves during decompression and coeval magma degassing:

$$\partial C_i / \partial t = \partial / \partial x [D_i(C) \partial C_i / \partial x], \qquad (1)$$

where C and D are the elemental concentrations in the embayment and the diffusion coefficient, respectively, and subscript i refers to the different volatile species. The diffusion equation is solved via a finite-volume approach. We assume that the diffusive volatile transfer is the only mass exchange in the embayment and that the host phenocryst does not undergo any further growth or exchange. The model is isothermal with a temperature of 1030 °C, based on olivine liquid thermometry between the MIs and host phenocrysts (Lloyd et al., 2013). In modeling the H_2O, CO_2 and S profiles, we take into account the effect of changing major-element composition on volatile diffusivities within the outer 20–40 micron chemical boundary layer adjacent to the bubble (e.g., Fig. 2). The diffusivities of all the volatile species are also dependent

on water concentration. We assume that diffusive loss from the embayment occurs only through the embayment outlet at the glass/bubble interface ($x = 0$). This assumption results in pressure- and time-dependent boundary conditions at the embayment exterior, while zero-flux conditions are prescribed at the inner-end of the embayment and distance L from the bubble. It is also assumed that the melt at the embayment terminus (i.e., adjacent to the vapor bubble), and the surrounding magma remains in equilibrium throughout the degassing process. We assume that the fully enclosed MIs trap melt at different depths in the conduit (Lloyd et al., 2013), and so define the degassing path taken by the melt exterior to the embayments. Diffusion is assumed to cease at a final pressure (P_F) at the time t_F when the magma abruptly cools, preserving the observed volatile zoning pattern:

$$C_{0,t} = C_{matrix}(p, t), \qquad (2a)$$

$$C_{0,tF} = C_{matrix}(P_F, t_F), \qquad (2b)$$

$$\partial C_{L,t} / \partial x = 0. \qquad (2c)$$

$C_{matrix}(p,t)$ is the volatile concentration of the matrix glass, which is pressure-dependent and, through the decompression rate, also time-dependent. As in previous embayment studies (Humphreys et al., 2008), we make the important assumption that the matrix melt is undergoing equilibrium degassing, consistent with the MI array (Lloyd et al., 2013). Prior to ascent, volatile species have flat profiles in the embayments and are in equilibrium with the matrix melt leading to the following initial conditions:

$$C_{x,0} = C_{matrix}(P_0), \qquad (3)$$

with $C_{matrix}(P_0)$ referring to the volatile concentration in the matrix at the initial pressure prior to ascent (P_0). The free parameters in this model that can be varied are the initial and final pressures, which control the initial and evolving exterior melt concentrations for all volatiles through a multi-element degassing model that is presented below. The other independent variable from these diffusion models is the decompression rate. Changes in the decompression rate dP/dt affect the shape of the diffusion profile and the extent of whole-embayment equilibration. Instead of iterating through many combinations of various P_0, P_F, and dp/dt, we constrain narrow bounds for reasonable P_0 and P_F through the embayment and MI volatile record as well as the multi-element degassing model, leaving only dP/dt as the primary free variable. We refined the grid spacing to between 1 and 2 μm after which no noticeable differences in the model results were observed. We use an implicit iteration scheme, which allows us to obtain accurate results even for large time stepping. However, to capture the time-dependent nature of the outlet boundary condition we use 200 time-steps. Further increases in the number of time-steps do not result in significantly different model outputs.

5.2. Fixing the initial and final pressures of magma degassing

One of the most essential starting conditions to define is the initial pressure (P_0) from where an embayment begins its ascent path. P_0 represents the starting pressure for the diffusion clock and ultimately determines the total distance the phenocryst travels from storage to eruption. P_0 may represent either the pressure of embayment formation during isobaric crystallization, or the pressure where the embayment last equilibrated with the external melt.

While choosing P_0 from the embayment records is non-unique, the MI population provides some guidance to the pressure range over which rapid crystal growth occurred. Inherent in this assumption is that embayments represent failed MIs and that both presumably share a common ascent history. Melt inclusions remain the premier tool for
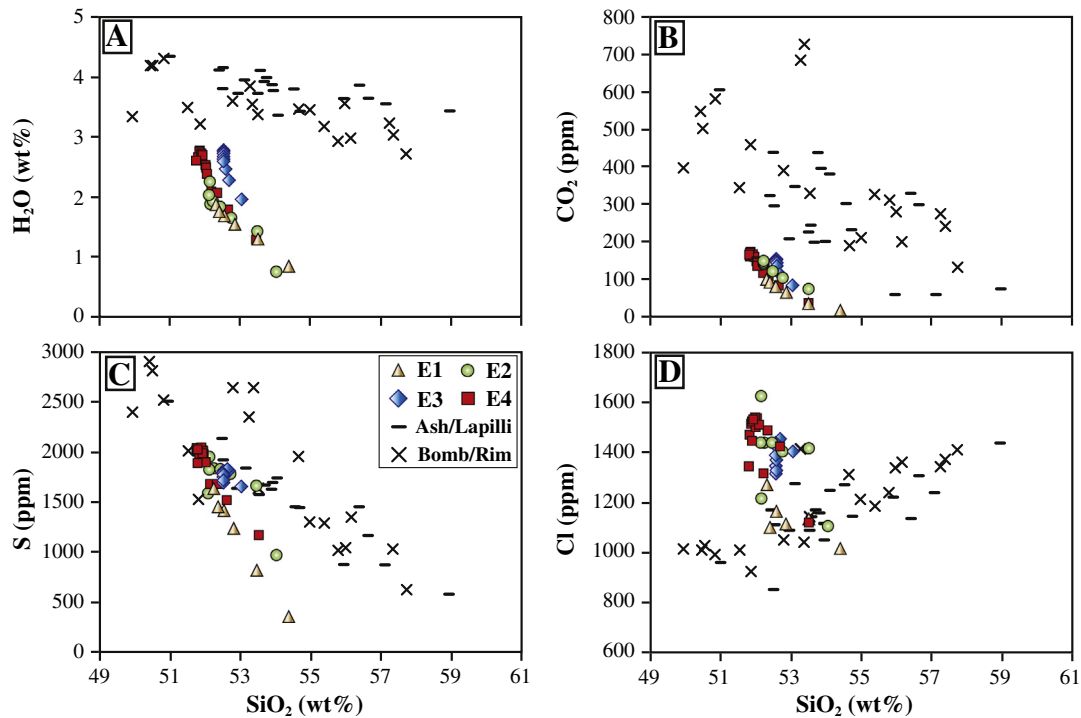
Fig. 4. Variations in volatile and SiO_2 concentrations in the Fuego embayments (colored symbols) and melt inclusions (crosses and dashes). Melt inclusion data are from Lloyd et al. (2013) and are split between fast-cooling (ash/lapilli — dashes) and slow-cooling (bomb/rim — crosses) eruptive products. Volatiles (H_2O, CO_2, S, and Cl) are measured by NanoSIMS or SIMS and SiO_2 is measured by EMP. For the embayments, SiO_2 concentrations are interpolated between analyses when the distance does not correspond to a NanoSIMS measurement location. (For interpretation of the references to color in this figure legend, the reader is referred to the web version of this article.)

tracking the degassing pathways for mafic magmas, despite their complexities (Metrich and Wallace, 2008). Some of the Fuego MIs, notably those derived from bomb-sized clasts and other small ones from lapilli, suffered H_2O-loss as a function of diffusive re-equilibration through the olivine host to the exterior degassing melt during ascent and/or post-eruptive cooling (Lloyd et al., 2013). These inclusions were corrected for H_2O-loss based on their K_2O content, and a model for coupled degassing and crystallization derived from the large, ash hosted MI and a numerical petrological model (Lloyd et al., 2013). When corrected, all of the Fuego MIs define a trend consistent with closed-system, vapor-saturated, equilibrium degassing path for H_2O, CO_2 and S (Fig. 5). The embayments fall off the closed-system degassing path due to substantial diffusive volatile loss of H_2O and CO_2, even from the interior of the embayments (Fig. 5A). On the other hand, the embayment interiors appear to retain their initial sulfur concentrations, as is evident in their overlap with the MI array (Figs. 3C and 4C). This is consistent with the lower diffusivity of sulfur compared to H_2O and CO_2 (see below) and hence potential to record P_0. We assume that the highest sulfur concentration in the embayments is representative of its initial value and, when combined with the H_2O–CO_2 and H_2O–S degassing path recorded in the MIs, constrains P_0 for the embayments. We develop a Fuego-specific, pressure-dependent H_2O–CO_2–S degassing model (Fig. 6) by combining a H_2O–CO_2 closed-system model (using a starting pressure of 400 MPa calculated from SolEx, Witham et al., 2012; Fig. 5A) with the H_2O–S degassing model (Fig. 5B) calculated in Lloyd et al. (2013). Essentially, these two degassing models are tied together through the H_2O content in the melt, and guided by the MI array. The combined model enables us to find a unique P_0 (and thus initial dissolved H_2O and CO_2 concentrations) for each embayment using the highest measured sulfur.

The pressure-dependent H_2O–CO_2–S degassing model was also utilized to constrain the external melt at the embayment outlet during ascent and decompression (Fig. 6). The deeper part (>150 MPa) of the closed-system degassing path is well constrained through the MI record

(Fig. 5A) and is primarily in the domain of CO_2 degassing. At pressures lower than 150 MPa, the degassing model mostly relies on the SolEx output as the MI record becomes sparse.

The final pressure (P_F) is interpreted to be the pressure at which the embayment glass quenches, presumably at shallow depths in the upper conduit (Humphreys et al., 2008). H_2O concentrations near the bubble and in the matrix glass provide the most robust constraint for P_F, since H_2O degassing continues to very low pressures (Fig. 6). The minimum H_2O measured in the embayments is 0.76 wt.% (sample 131-E1) corresponding to a pressure of 6 MPa, based on SolEx (this is an upper limit as H_2O was measured ~5 μm from the bubble in an area of a steep concentration gradient). The four embayments show similar H_2O-profiles approaching the bubble, consistent with equilibrating lastly with a melt containing ~0.4 wt.% H_2O (P_F ~2 MPa), which is higher than the concentration of H_2O measured in the degassed groundmass glass (0.042–0.057 wt.% H_2O; Supplementary Table 5).

5.3. Volatile diffusivity

Any diffusion chronometer depends critically on the diffusivity for the species of interest, which may vary as a function of temperature, pressure, and melt composition (Costa and Morgan, 2010; Zhang and Cherniak, 2010). Below we outline the composition-dependent diffusion coefficients that we use specific to the Fuego basaltic andesitic melts at a constant temperature of 1030 °C.

The diffusivity of H_2O in silicate melt is relatively well-characterized in comparison to the other volatile species (Zhang and Ni, 2010 and references therein). The temperature dependence of H_2O is defined by an Arrhenius relationship with similar activation energy for different magma compositions (Fig. 7). We ignore pressure effects on the diffusivity of H_2O, which are minor for intermediate to mafic melt compositions like at Fuego (Behrens et al., 2004; Zhang and Ni, 2010). D_{H2O} in silicate melt is known to be strongly dependent on melt composition,
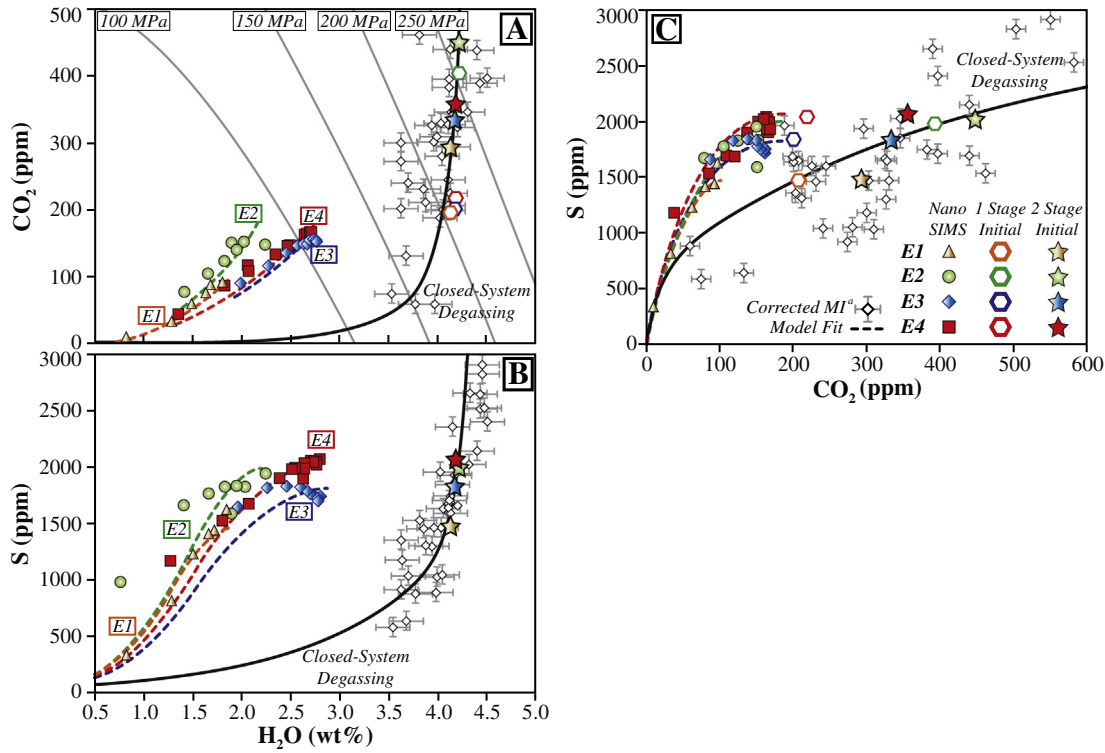
Fig. 5. H_2O, CO_2, and S systematics in the Fuego embayments (colored symbols) and melt inclusions (open diamonds). The 1 RSD error bars and melt inclusion (MI) data are from Lloyd et al. (2013), and include those MI corrected for H_2O-loss. Initial concentrations in the embayments are given as open hexagons for the single-stage model (allowing for best-fit CO_2) and stars for the two-stage model (derived from closed-system degassing models, shown as black lines through the MIs). Colored lines are decompression–diffusion model fits to the two-stage decompression model (Table 3b, Fig. 11). A) The closed-system degassing path was generated by SolEx (Witham et al., 2012). Isobars were generated by VolatileCalc (Newman and Lowenstern, 2002). 6 MIs have greater than 500 ppm CO_2 and are not plotted but correspond to formation depths >300 MPa. B) The closed-system degassing line shows a fractionation model for simultaneous H_2O and S equilibrium degassing following the methods of Sisson and Layne (1993); with the following parameters: $H_2O_{initial}$ = 4.30 wt.%, $S_{initial}$ = 3000 ppm, $Kd_S^{vap/liq}$ = 90, and H_2O is 8% of the non-liquid separating assemblage (e.g., crystals and vapor), with shallow degassing constrained to intersect the groundmass value. C) The closed-system degassing path is a combination of the degassing trends calculated from the methods presented in A and B. (For interpretation of the references to color in this figure legend, the reader is referred to the web version of this article.)

with diffusivities in basalt being a factor of 10 greater than in andesite at the same temperature (Fig. 7; Zhang and Ni, 2010). The embayments in this study fall within this compositional range, although a simple average is likely inadequate for the Fuego basaltic andesite. D_{H2O} is primarily dependent on melt SiO_2 content, however, alkaline components and non-SiO_2 network formers are known to have significant effects as well (Okumura and Nakashima, 2006; Ni et al., 2013). Because Fuego erupts a high-alumina basaltic andesite, the effect of the Al_2O_3 concentration, in particular, needs to be assessed.

To account for the extent of melt polymerization, we parameterized D_{H2O} using NBO/T, the ratio of non-bridging oxygen to tetrahedrally coordinated cations that act as network formers (calculated by methods outlined in Mysen and Richet, 2005). Although the average SiO_2 concentration in the Fuego magma (52.8 wt.%) is closer to typical basalts (≤52 wt.%) than andesites (≥57 wt.%), the NBO/T ratio indicates that melt polymerization for the Fuego embayments is more similar to the andesitic melt studied by Behrens et al. (2004) (Fig. 8). As shown previously (Fig. 2), the Fuego embayments are zoned in their major elements with greater melt polymerization (a decrease in NBO/T) near the bubble, effectively lowering D_{H2O} at the outlet (Fig. 8). We approximate D_{H2O} in Fuego embayments via a linear interpolation of D_{H2O} and NBO/T between andesitic and basaltic melt (Fig. 8 inset). The four embayments show similar NBO/T zoning patterns that are fitted with a logarithmic regression as a function of distance from the bubble (see Fig. 8). In addition to adjusting D_{H2O} for variations in major elements, D_{H2O} is also dependent on the concentration of the H_2O dissolved in the melt, being a factor of 5 lower in melt containing 4 wt.% H_2O vs. a completely dry melt (Fig. 7 inset). By combining the logarithmic

regression and the relation between NBO/T and D_{H2O}, we calculate D_{H2O} as a function of distance from the bubble:

$$D_{H_2O} = C_{H_2O} \exp\left(-8.56 - \frac{19110}{T}\right) \bullet (0.057 \ln(X) + 0.0732) \quad (4)$$

where D_{H2O} is in m^2/s, C_{H2O} is wt.% H_2O, T is in K, and X is the distance in μm from the bubble. We incorporate these compositional and temperature dependences in the decompression model, by allowing for a spatio-temporally variable D_{H2O}. The parameterization we developed here leads to diffusivities that are within the $+/-0.2$ log unit uncertainty of the viscosity-based model of Persikov et al. (2010). This is no surprise, as their model in the region of interest is also highly constrained by the same experimental diffusivities we use here (Behrens et al., 2004; and Zhang et al., 2007), and melt viscosity is highly related to NBO/T.

Because the diffusion of CO_2 in silicate melt has been shown to be relatively independent of speciation and anhydrous melt composition (Nowak et al., 2004), CO_2 diffusion is less complicated than H_2O diffusion. The diffusivity is well characterized for Fuego melts with a pressure- and H_2O-dependent Arrhenius equation (Fig. 7; Zhang et al., 2007):

$$D_{CO_2} = \exp\left(-13.99 - \frac{17367 + 1944.8P}{T} + \frac{(855.2 + 271.2P)}{T}C_{H_2O}\right) \quad (5)$$

where D_{CO2} is in m^2/s and P is in GPa.

In comparison, sulfur diffusivity (D_S) in silicate melts is poorly understood not only because of the limited number of studies, but
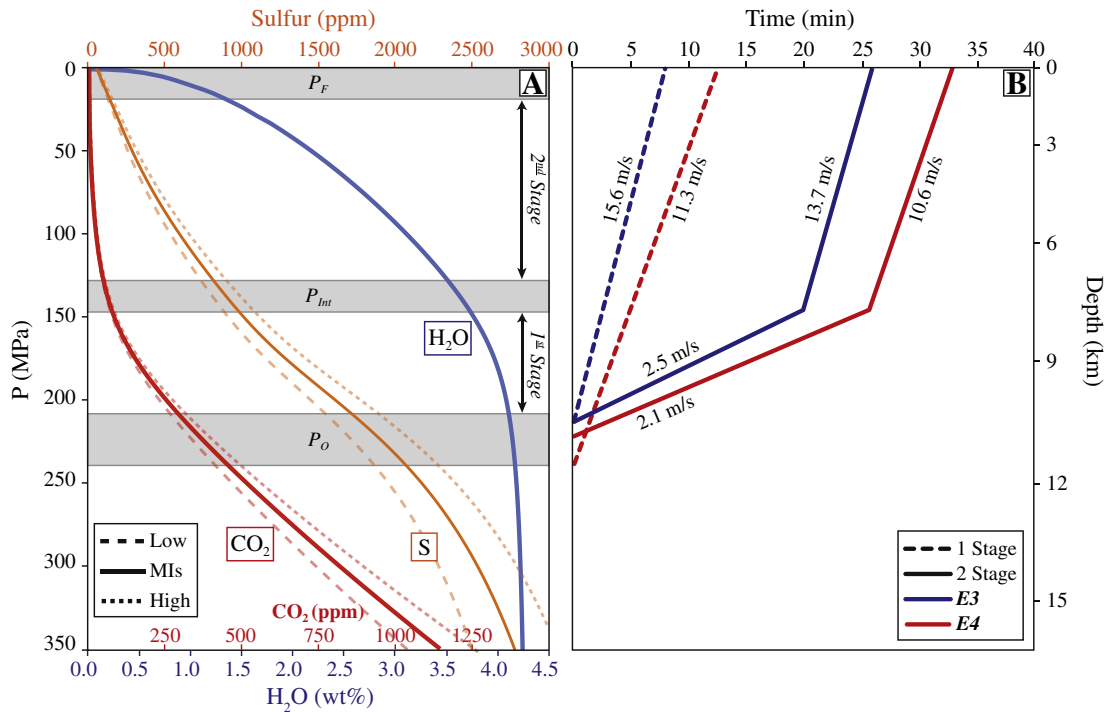
Fig. 6. A) H_2O–CO_2–S degassing model used for determining P_0, initial H_2O and CO_2 for the embayments, and evolving volatile concentrations as a function of P in the exterior melt. Curves are the closed system degassing paths defined by the MI population presented in Fig. 5. Note all volatiles have independent axis scales. Gray bars represent the range P_0, P_{Int}, and P_F assumed for the two-stage model. The first stage of slower decompression occurs between P_0 and P_{Int} and the second stage between P_{Int} and P_F. The dotted lines represent $+/-$ 10% uncertainties applied to the degassing models (Table 3b). B) A comparison of calculated ascent rates for the single-stage and two-stage models. E1 and E2 are omitted for clarity purposes. Ascent rate was calculated directly from decompression rate estimates derived from the embayment diffusion models (Table 3b). Note that the depth axis is non-linear because density varies with depth (see text for conversion from pressure to depth). The increase in ascent rate for the two-stage model could coincide with the start of rapid H_2O exsolution at P_{Int}, reflecting a change in velocity as the bubble fraction in the magma increases.
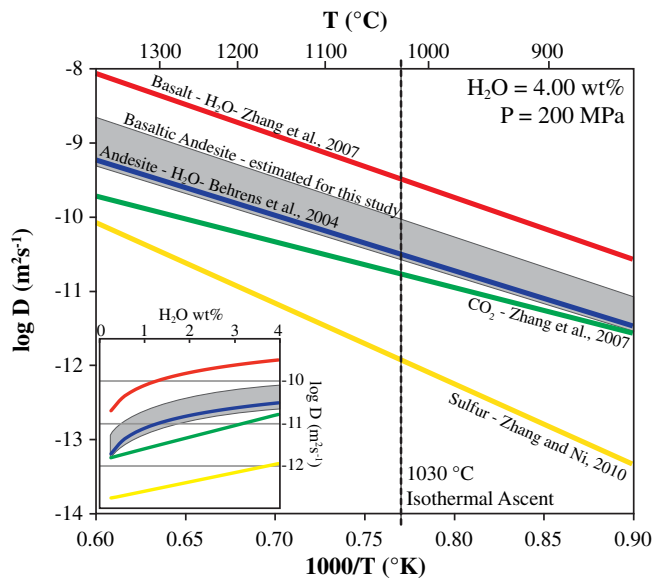
Fig. 7. Arrhenius plot illustrating D_{H_2O}, D_{CO_2}, and D_S in melt with 4 wt.% H_2O at a pressure of 200 MPa (similar to the initial conditions for the Fuego embayments). D_{H_2O} is known to be highly dependent on major element melt composition. Because Fuego melt compositions fall between basalt and andesite, D_{H_2O} was interpolated from those compositions (see Fig. 8). The inset shows the effect of decreasing dissolved H_2O on D_{H_2O}, D_{CO_2}, and D_S at a temperature of 1030 °C and 200 MPa (with the same color code and model as referenced). Both the major-element composition of the melt and the concentration of dissolved H_2O have an order of magnitude effect on D_{H_2O} and both are taken into account in the diffusion modeling. (For interpretation of the references to color in this figure legend, the reader is referred to the web version of this article.)

also because of the possible variation in diffusivity of different S species as a function of fO_2 (Zhang et al., 2010). Nonetheless, existing experiments show no strong fO_2 dependence, perhaps due to the predominance of melt viscosity over speciation on S diffusivity (Behrens and Stelling, 2011). We use an Arrhenius equation derived from experiments conducted on Etna and Stromboli basalts for temperature, pressure, and H_2O concentrations that are relevant to the Fuego magma (Fig. 7, Zhang et al., 2007):

$$D_S = \exp\left(-8.21 - \frac{27692 - 651.6 C_{H_2O}}{T}\right) \qquad (6)$$

where D_S is in m^2/s. In these experiments the oxygen fugacity was 3 log units below QFM and sulfur was present primarily as sulfide. Though rare sulfide blebs have been observed as inclusions in phenocrysts associated with this eruption, the fO_2 in this experiment is much lower than the estimated oxygen fugacity in the Fuego magma (fO_2 ~ QFM + 1; Lloyd et al., 2013). With a lack of experiments on more oxidized systems, and with the limited effects that have been observed thus far as a function of fO_2, we use this sulfide-dominant Arrhenius equation.

5.4. Single-stage decompression

We first consider whether the simplest case, a single-stage, constant decompression rate can produce appropriate profiles for all three volatile species, given the diffusivity models and initial condition constraints outlined above. In this single-stage decompression scenario, it was assumed that each phenocryst host had fully formed an embayment and was residing at P_0. As outlined above, the maximum S concentration of the inner, flat portion of each embayment was used to define
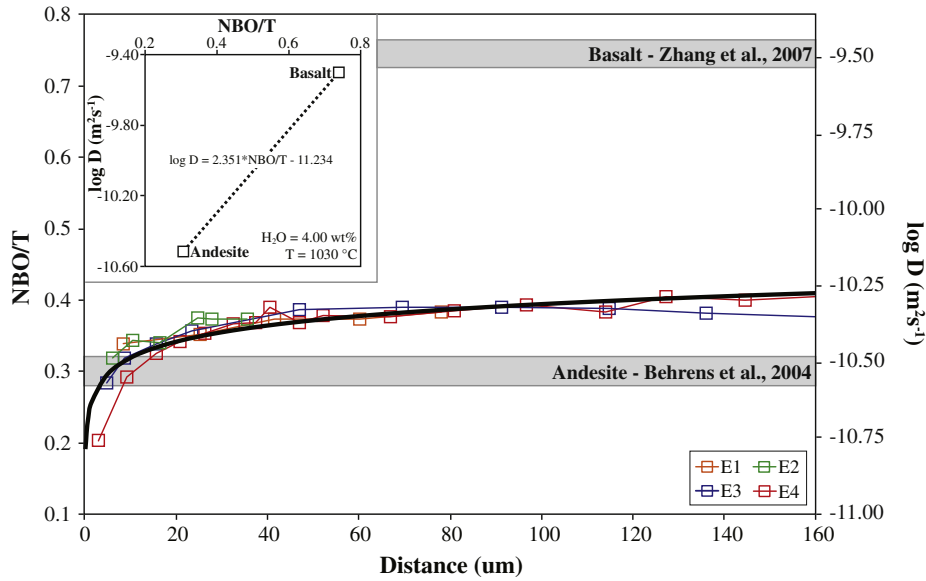
Fig. 8. Compositional variations along the embayments, plotted as non-bridging oxygen to tetrahedrally coordinated cations (NBO/T) as a function of distance from the bubble. The gray bars represent the NBO/T ratios for basalt and andesite compositions used as starting material for water diffusion experiments (references as given). The inset graph shows the linear interpolation between these two compositions and D_{H2O} (for 4 wt.% H_2O at 1030 °C). This model was used along with the parameterizations for temperature and water shown in Fig. 7, to calculate D_{H2O} in Fuego embayments with distance from the bubble (Eq. (4)).

the values for P_0, initial H_2O, and initial CO_2 derived from the multi-element degassing model in Fig. 6. Then the system was decompressed at a constant rate until P_f was reached, driving the exterior melt to degas (again, following Fig. 6), and causing the volatiles within the embayment to diffuse to the boundary, where concentrations are lower. The only free variable used to fit the diffusion profiles was the decompression rate.

We first modeled H_2O, because it has a well-characterized diffusivity and a nearly constant initial value (~4.2 wt.%). The fits to H_2O using this single-stage model are excellent (Fig. 9A) and yield a narrow range of decompression rates for all embayments, from 0.32 to 0.47 MPa/s, for total ascent times ranging from ~8 to ~12 min from 191 to 238 MPa (Table 3a). The best fit was determined by minimizing the root mean square (RMS) error, which were all less than 2 RSD of the maximum
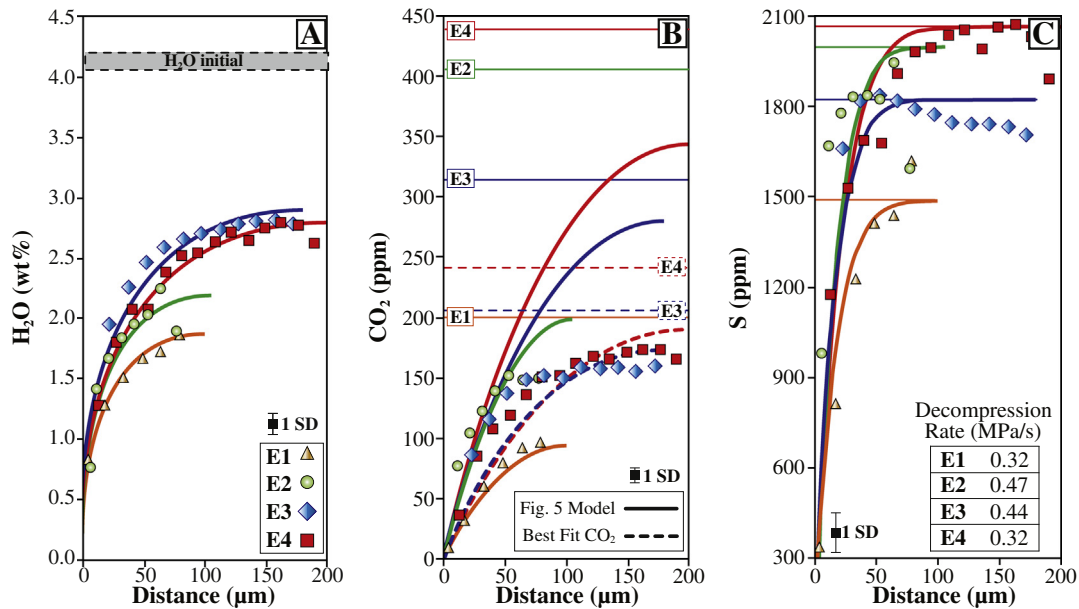
Fig. 9. Best fit decompression–diffusion models (colored lines) to measured volatile concentration profiles (symbols) in four melt embayments, using the degassing model in Fig. 6, the initial concentrations in Fig. 5, and the diffusivities in Figs. 7 and 8. All models consider a constant decompression rate from P_0 to P_f (values given in Table 3a). Volatile concentrations are plotted as distance from the bubble. A) H_2O is fit well with a narrow range of decompression rates for all four embayments, and has correspondingly low RMS misfit values (Table 3a). All embayments start with the same initial H_2O within the values of the gray bar (~4.2 wt.%). B) Using the same decompression rates as determined for H_2O, CO_2 is not fit successfully with the degassing model in Fig. 6 and initial values shown as solid colored lines. Dashed lines show better fits if the initial CO_2 concentrations are allowed to freely vary from those defined by the average MI array (see Fig. 5). C) The same decompression rates determined for H_2O provide excellent fits to sulfur in E1 and E4 embayments, but not in E3 and E2, which have complex shapes. Initial sulfur values are equal to the interior concentrations. See Table 3a for all parameters. (For interpretation of the references to color in this figure legend, the reader is referred to the web version of this article.)

Table 3

a: Single-stage decompression

Emb.	H_2O_0 (wt.%)	CO_2 (ppm)	S_0 (ppm)	P_0 (MPa)	P_F	H_2O (wt.%)	RMS CO_2 (ppm)	S (ppm)	Decompression rate (MPa/s)	Time (min)	Ascent velocity (m/s)
E1	4.09	218	1474	191	2	0.10	9	102	0.32 *(0.24–0.42)*	10.2 *(7.7–13.6)*	11.0 *(8.3–14.4)*
E2	4.20	406	1986	232	2	0.15	24	299	0.47 *(0.35–0.60)*	8.4 *(6.6–11.3)*	16.5 *(12.3–21.1)*
E3	4.16	314	1771	213	2	0.11	89	124	0.44 *(0.36–0.55)*	8.4 *(6.7–10.3)*	15.6 *(12.3–18.8)*
E4	4.21	439	2049	238	2	0.08	126	110	0.32 *(0.27–0.38)*	12.6 *(10.7–15.0)*	11.3 *(9.5–13.3)*

b: Two-stage decompression

Emb.	H_2O_0 (wt.%)	CO_2 (ppm)	S_0 (ppm)	CO_2 factor	S factor	P_0	P_{INT} (MPa)	P_f	H_2O (wt.%)	RMS CO_2 (ppm)	S (ppm)
E1	4.13	292	1479	High	Low	202	145	2	0.09	5	92
E2	4.20	447	1986	High	Norm	232	145	2	0.15	23	316
E3	4.16	314	1771	Norm	Norm	213	145	2	0.12	24	197
E4	4.18	354	2057	Norm	High	221	145	2	0.08	16	94

Emb.	Decompression rate		Time		Ascent velocity	
	1st stage	2nd stage	1st stage	2nd stage	1st stage	2nd stage
	(MPa/s)		(min)		(m/s)	
E1	0.19	0.32	5.1	7.7	8.2	9.9
E2	0.28	0.47	5.2	5.3	11.7	14.7
E3	0.06	0.44	20.3	5.6	2.5	13.7
E4	0.05	0.34	25.8	7.3	2.1	10.6

Initial conditions and model output for the single- (a) and two-stage (b) decompression (as in Figs. 9 and 11, respectively). The mean ascent velocity in the two-stage model refers to the velocity calculated from P_0 to P_F and is essentially the time-weighted mean value for the 1st and 2nd stages. Italicized numbers in parenthesis represent the range of accepted values taking into consideration the errors in the NanoSIMS measurements (Fig. 12). Based on the variability within the MI population, the degassing models were allowed to vary by 10% in order to reduce the RMS error values and achieve more uniform decompression rates across the embayments. For example, in comparison to E3, E4 has a similar length scale, CO_2, and H_2O concentrations but is clearly enriched in terms of sulfur. For this reason, the sulfur degassing model was increased by a uniform 10% relative to the corresponding pressure when modeling E4 in order to compensate for this enrichment (see Fig. 6a). A 10% enriched correction is denoted by the term "high" and a 10% depleted correction is denoted by the term "low".

measured H_2O (0.18 wt.% H_2O; Table 3a). The same decompression rates that fit the H_2O profiles also provide adequate fits for sulfur (Fig. 9C), although the shapes of the profiles do not match the curvature of the concentration profiles in all cases (E2 and E3). Indeed, the increase in S toward the bubble in embayment E3 can only be modeled with uphill diffusion or some more complex change in the diffusivity or solubility. Given these uncertainties in sulfur behavior, and the likely changes in fluid-melt partitioning (Fiege et al., 2014) or speciation (Kelley and Cottrell, 2012) that could affect diffusion during degassing, we consider these fits successful in matching both H_2O and S profiles with the same decompression rate. This is especially notable given the greater than two orders of magnitude difference in their diffusivities.

On the other hand, we were not able to fit the CO_2 profiles for all the embayments, using the initial values predicted from the S–CO_2 solubility relationship in Fig. 5. The fits to the two shorter embayments (E1 and E2) were satisfactory, but the innermost CO_2 concentrations predicted for the two longer embayments were greatly in excess of the measured values (i.e., 250–350 vs. ~150 ppm). Given the intermediate diffusivity for CO_2, the short time constrained by the H_2O profiles (~10 min), and the high initial concentrations (i.e., 300–450 ppm CO_2), there is not enough time for the re-equilibration of CO_2 in the long embayments (E3 and E4). Thus, the only solution to match the CO_2 profiles given a constant decompression rate model is to impose lower initial CO_2 concentrations of 200–250 ppm. This combination of high S (1800–2000 ppm) and low CO_2 (<250 ppm) concentrations is not a common occurrence in the Fuego MI population, although it has been observed in some experimental studies (Lesne et al., 2011). On the other hand, syneruptive processes such as CO_2 gas fluxing (Blundy et al., 2010), non-equilibrium CO_2 degassing during rapid ascent (Pichavant et al., 2013), or non-equilibrium sulfur degassing (Fiege et al., 2014) can be invoked to explain the deviations from a closed-system degassing path. Therefore, we cannot exclude the possibility that these embayments started with lower CO_2 than typical of the MI S–CO_2 array. If that were the case,

then all three volatiles and four embayments can be modeled with a constant decompression rate of ~0.4 MPa/s and total ascent time from ~9 to 12 km depth in less than 12 min.

5.5. Two-stage decompression

Given the difficulty in fitting the CO_2 concentrations with a single-stage model, we considered the possibility that the embayments ascended in two stages, with an initial slow decompression (first stage) and a relatively faster decompression as the magma nears the surface (second stage). In this scenario, the intermediate pressure at which the magma transitions from a slower to faster decompression rate, P_{Int}, has to be chosen. This proposed second stage presumably coincides with the onset of H_2O degassing. This is a feature of any closed-system degassing path, where CO_2 is almost entirely lost before major H_2O degassing begins (Figs. 5, 6). Thus the two volatile species are sensitive to different parts of the system, and the two-stage model exploits this feature to better constrain how the decompression rate may vary with depth.

Because we have no physical constraint on P_{Int}, we first explored its possible range using a single embayment, E4. Although E4 is an embayment extracted from the interior of a slowly cooled bomb, which may have experienced additional time at high temperature during post-eruptive delayed cooling (Lloyd et al., 2013), it displays the most systematic profiles in H_2O, CO_2, and S. We obtained P_0 using the S-based method outlined above, and then allowed P_{Int} and the decompression rate to vary independently. Our first observation was that the second stage decompression rate (0.32 MPa/s) is well-constrained by H_2O and remains constant for all P_{Int} values (Fig. 10C). This implies that the majority of H_2O re-equilibration is occurring at shallow depths (after P_{Int}), which is consistent with the fact that H_2O does not degas significantly until <150 MPa (Fig. 6). On the other hand, there is no unique solution for the first, deep stage because P_{Int} and dP/dt trade-off to permit similar timescales for CO_2 re-equilibration (Fig. 10C). There is an upper limit to
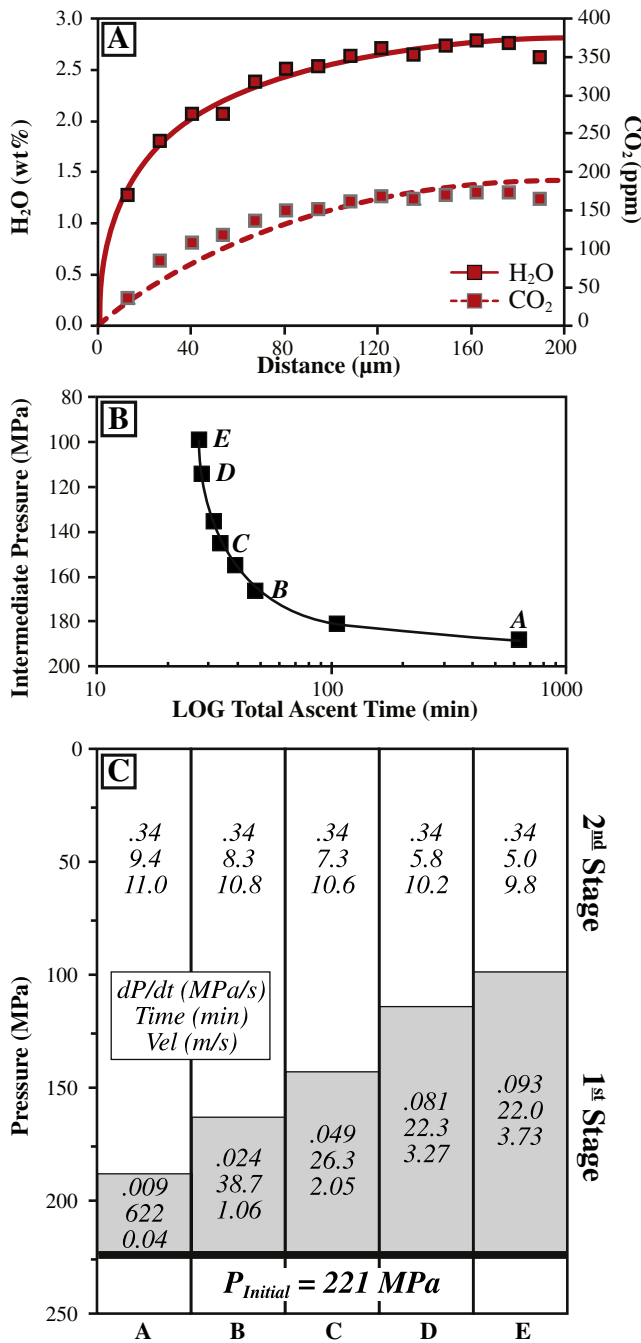
Fig. 10. Trade-off between P_{int} and decompression rate in a two-stage model (i.e., P_0–P_{int} is the first stage, and P_{int}–P_f is the second). A) Decompression–diffusion model (colored lines) fits to E4 embayment H_2O and CO_2 data (colored symbols) for the 5 two-stage scenarios presented in panels B and C (RMS errors in Table 3b). B) P_{Int} vs. the total ascent time predicted by the two-stage model. As P_{Int} decreases, the total ascent time also decreases. The two-stage model can no longer produce the diffusion curves in panel A at P_{Int} >185 MPa (scenario A) or P_{Int} <100 MPa (scenario E), for reasons outlined in the text. C) Parameters for the five scenarios that produce the fit observed in panel A. The first stage is largely controlled by the shape of the CO_2 profile. As P_{int} decreases (CO_2 concentration drops in the exterior), the decompression rate in the first stage increases (to prevent too much loss of CO_2). The decompression rate in the second stage is largely controlled by the H_2O profile, which is unaffected by the ascent history at P_{Int} >145 MPa (see Fig. 6). (For interpretation of the references to color in this figure legend, the reader is referred to the web version of this article.)

P_{Int} at around 185 MPa, where the dissolved CO_2 concentration in the decompressing magma is ~250 ppm (Fig. 6), which is too high to create a flat plateau in the inner embayment of ~175 ppm (Fig. 10A). For this

reason we consider 185 MPa to be the maximum P_{Int}, and the corresponding total ascent time of ~10 h to be the maximum for the two-stage scenario. At the other limit, as P_{Int} shallows, an increase in decompression rate is needed to compensate for the increasing concentration gradient between CO_2 in the embayment and in the exterior melt. At pressures less than 140 MPa, the dissolved CO_2 in the decompressing magma approaches concentrations less than 65 ppm, and embayment re-equilibration is relatively insensitive to further decreases in CO_2 solubility. This asymptotic limit at lower P_{Int} (Fig. 10B) results in a minimum total ascent time of ~30 min.

Although this experiment with E4 demonstrates how a range of P_{Int} results in good fits, we modeled the other embayments using a constant value for P_{Int} of 145 MPa (Table 3b). This value is guided by both observed MI entrapment pressures and what might plausibly control P_{Int} dynamically. The Fuego MIs were likely trapped by a slow crystal growth mechanism as they do not exhibit the textural characteristics of fast dendritic growth (Faure and Schiano, 2005). If we interpret this slow crystal growth to occur prior to or during the first, slow stage of decompression, then the MI with the shallowest entrapment pressure would represent the transition to the second, faster stage of decompression. In this case, the MI with the lowest S (our proxy for P_0 in this study) corresponds to an entrapment pressure of 145 MPa (calculating solubility pressure from H_2O and CO_2 and VolatileCalc, Newman and Lowenstern, 2002; see also Fig. 5). This pressure also coincides physically with where the decompressing magma starts to lose significant H_2O, which being the major volatile species, will dominate the buoyancy and thus ascent of the system (Mastin and Ghiorso, 2000). Thus, given that there is a clear change at ~145 MPa both in the melt inclusion population, and in the predicted mass fraction of vapor in the system, we use this value of P_{Int} for the remaining embayment calculations.

The results of fitting all the embayments with two stages of decompression are shown in Fig. 11. Unsurprisingly, the decompression rate for the second, shallow stage of ascent is identical to that what was calculated for the single-stage model (Table 3b), because both are dominated by H_2O-loss. The decompression rate for the first, deep stage of ascent is then constrained by CO_2. With additional time to reequilibrate, higher initial CO_2 concentrations are permitted, which is more consistent with the H_2O–CO_2–S degassing model defined by the MIs (Fig. 5). As a result of the slower initial ascent, there is also a noticeable decrease in the RMS error for S in the two embayments exhibiting systematic S profiles (110 to 94 ppm for E4 and 102 to 92 ppm for E1). This improvement in fit is a result of the additional time at increased concentrations of S and aids in recreating the inflection of the measured S concentrations between a distance of 40 and 70 μm from the bubble (Fig. 11C). In the case of the two longer embayments that were not fit well by the single-stage scenario (E3 and E4), decompression rates for the initial stage of ascent are an order of magnitude slower (~0.05 MPa/s) than those calculated for the second, more rapid stage of ascent (~0.4 MPa/s). This has the effect of increasing the total ascent time by 15 to 20 min (Table 3). Although the two shorter embayments (E1 and E2) were fit relatively well with the single-stage scenario, increasing the total ascent times by ~3 min further improves the fits.

In summary, a constant decompression rate scenario predicts rates between 0.3 and 0.5 MPa/s and total ascent times between 8 and 12 min, but requires some ad hoc adjustments to the initial CO_2 concentrations of the different embayments. If decompression is split into a slower and faster regime, with the transition occurring around 150 MPa, total ascent times between 10 and 35 min produce higher quality fits to the data, with a single H_2O–CO_2–S degassing model. Because the first stage of the two-stage scenario cannot be solved uniquely (Fig. 10), we cannot exclude the possibility that there is a slower decompression event at depth that could take up to 10 h. However, at pressures below 150 MPa, the decompression rate is well-determined and fast (0.3–0.5 MPa/s and 8–12 min in duration) and may be more relevant to the dynamics of the eruption.
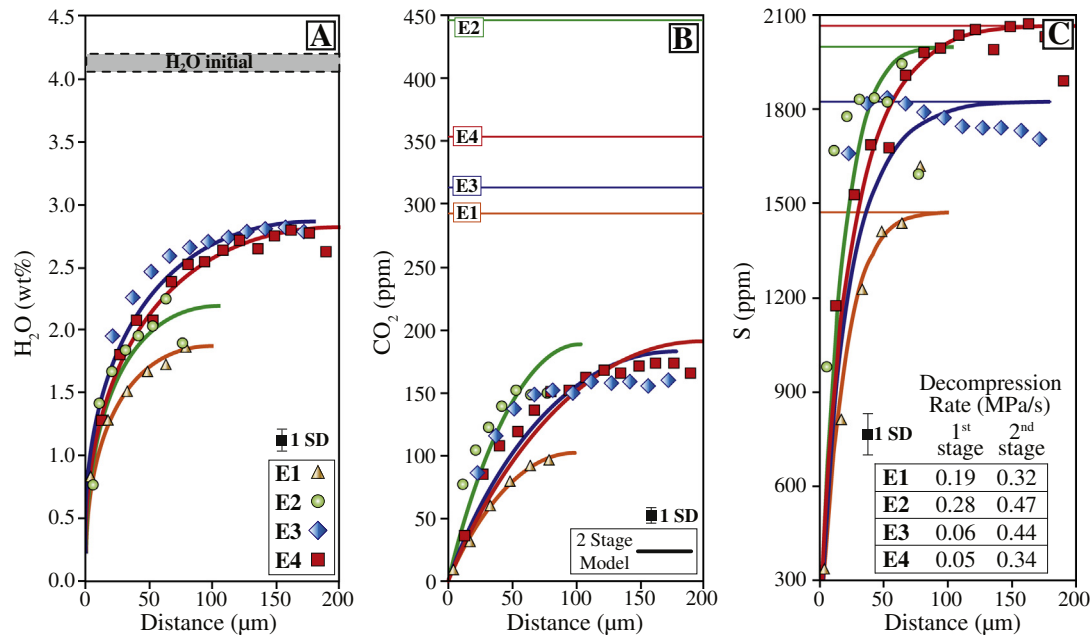
Fig. 11. Best fit decompression–diffusion models (colored lines) to measured volatile concentration profiles (symbols) in four melt embayments, using the degassing model in Fig. 6, the initial concentrations in Fig. 5, and the diffusivities in Figs. 7 and 8. All models are for two stages of decompression, as in Fig. 10, with P_{int} at 145 MPa. Volatile concentrations are plotted as distance from the bubble. A) H_2O is fit well with similar rates to the constant decompression model, because it is not degassing during the first-stage (Fig. 6). B) The fits to CO_2 are improved, and the initial concentrations are more similar to each other, relative to the single stage models in Fig. 9. C) The fits are improved slightly for E1 and E4 (i.e., lower RMS misfit) relative to the single-stage model. See Table 3b for all parameters and results. (For interpretation of the references to color in this figure legend, the reader is referred to the web version of this article.)

5.6. Calculating depth and ascent rate

We use the method outlined in Humphreys et al. (2008) to convert decompression rate to ascent velocity, which uses a magma density model that incorporates the effects of bubble exsolution and 40% pre-existing phenocrysts in the magma column (Wilson et al., 1980):

$$\rho = \left[\left(\frac{1-n}{\rho_m}\right) + \left(\frac{nRT}{P}\right)\right]^{-1} \qquad (7)$$

where ρ_m is the bubble-free, hydrous magma density (2450 kg/m³), n is the mass fraction of exsolved volatiles (7% at P_0 and 60% at P_F based on output from SolEx; Witham et al., 2012), R is the gas constant and P is the pressure. Density was calculated by averaging the embayment compositions from Table 1 and assuming 4.20 wt.% H_2O (major-element volume and thermal expansion data from Lange and Carmichael (1987) and H_2O from Ochs and Lange (1999)). The ascent velocity (v) is then calculated from:

$$v = \frac{1}{t}\left(\frac{P_i}{\rho_i g} - \frac{P_f}{\rho_f g}\right) \qquad (8)$$

where g is the gravitational acceleration (9.81 m/s²) and t is the duration of the model. Ascent velocities range from 11.0 to 16.5 m/s in the case of constant decompression (Table 3a) and 2.1 to 11.7 m/s and 9.9 to 14.7 m/s for the first and second stages respectively (Table 3b). If the volcanic conduit was assumed to be lithostatic (assuming a crustal density of 2700 kg/m³), the calculated ascent velocities would decrease by <2 m/s.

5.7. Effect of differential clast cooling

In our previous study (Lloyd et al., 2013), we demonstrated that MIs from bomb-sized clasts lost H_2O in comparison to MIs from ash and lapilli. A conductively cooled 6-cm volcanic bomb will remain at high temperatures and open to diffusion for an additional 5–10 min after

eruption. The observed diffusive re-equilibration in the bomb MIs could occur in this timeframe only for the fastest laboratory measurements of D_{H2O} in olivine. For more representative D_{H2O}, the bomb MI would require additional time at high temperature, perhaps in the upper conduit during post-fragmentation comminution or as a result of slower ascent (Lloyd et al., 2013). E4 is an embayment from a volcanic bomb, and both single- and two-stage decompression models predicted longer equilibration times than the embayments in the ash and lapilli samples (i.e., a difference of ~5 min for the single-stage model and ~20 min in the two-stage scenario). Although some of this additional time results from the higher P_0 predicted for the bomb embayment (due to its higher initial sulfur), the rest could derive from conductive cooling post-eruption.

It may also be significant that the two embayments from ash-sized clasts (E2 and E3) yield the highest ascent velocities and shortest rise times for both models (Table 3). Lloyd et al. (2013) had speculated that ash-sized fragments might preferentially form from portions of magma that ascend more rapidly, due to contrasts in bubble number density, crystallinity or other aspects of their physical properties. More rapid ascent rates for the ash-hosted embayments are also suggested from their sulfur profiles. If the interior of all the embayments is unaffected by diffusion of sulfur, then the length scale of the outer gradient should scale with the diffusive timescale. Combined NanoSIMS and EMP profiles (Supplementary Table 2) show that such outer sulfur boundary layers are shortest (25–30 μm) for ash-hosted embayments, longer for the lapilli-hosted embayment (40–50 μm), and longest for the bomb-hosted embayment (75 μm). While this is consistent with faster decompression for the ash-hosted embayments, the length scales of the sulfur profiles are too short to be consistent with the decompression rates calculated from the H_2O profiles. This is apparent in Fig. 11, where the diffusion profiles derived from H_2O provide poor fits to S profiles in embayments E2 and E3. It is also noteworthy that S does not vary monotonically in these embayments, but undergoes an increase toward the outlet before sharply declining. Thus, the shape and length of the outer sulfur boundary layer in E2 and E3 may reflect enrichment from the thinning embayment neck or other processes than diffusive loss

during ascent, such as non-equilibrium effects related to changing sulfate solubility as a function of pressure (Fiege et al., 2014). Thus, although there may be some different processes and rates accompanying the embayments from different clasts, the results from the four embayments are remarkably similar. A larger number of embayments from a greater variety of clast sizes would be necessary to isolate those effects due to variable cooling and ascent rates as a function of clast size.

5.8. Implications for the 1974 Fuego eruption

The decompression rates determined here are the first for the 1974 eruption of Fuego, but they can be compared to previous magma supply rate estimates. Based on the volume flux of erupted material, Rose et al. (2008) estimated a magma eruption rate of 3.2×10^6 kg/s for the October 14 phase of the eruption. Because the October 17 phase was observed to be 30% larger than the initial phase, we consider a magma supply rate of 10^6 kg/s to be a minimum for this day of the eruption. A simple mass balance calculation can relate ascent rate to mass eruption rate for an assumed conduit dimension (Rutherford, 2008):

$$M = \pi r^2 \rho_F v \qquad (9)$$

where M is the mass eruption rate (kg/s), r is the conduit radius, ρ_F is the dense rock equivalent density of the Fuego magma (2750 kg/m^3, Rose et al., 2008), and v is the velocity (m/s). More recent explosive eruptions at Fuego (May 1999 and September 2012) have created crater radii on the order of 40 to 65 m, which could be connected to a conduit with an order of magnitude smaller radius (Escobar, pers. comm., 2013). Given a range of mass eruption rates between 3×10^6 and 6×10^6 kg/s and a reasonable range of conduit radius, the corresponding range of ascent rates calculated by mass balance is 14 to 28 m/s for a 5 m conduit and 3.5 to 6.9 m/s for a 10 m conduit radius, which are comparable with the range of ascent rates calculated for this study (Table 3). Cashman (2004) also identified a range of decompression rates for sub-Plinian eruptions between 0.01 and 1 MPa/s, which also are consistent with the calculations from this study (~0.3 to 0.5 MPa/s in the upper ~7 km).

Following the development in Qin et al. (1992), several recent studies have used fully-enclosed, olivine-hosted melt inclusions to constrain magma ascent based on the diffusive equilibration of H_2O through olivine (Chen et al., 2013; Lloyd et al., 2013). H_2O diffusion in olivine has larger uncertainties than that in melt. Experimental determinations of H^+ diffusion coefficients in olivine span at least three orders of magnitude (Farver, 2010), due to multiple proposed mechanisms that may dominate under different fO_2 and fH_2O regimes (Kohlstedt and Mackwell, 1998). For the October 17 MIs, estimates for ascent span more than an order of magnitude based on the assumed diffusion mechanism in olivine (Lloyd et al., 2013), from <12 m/s if the fast redox mechanism dominates (Kohlstedt and Mackwell, 1998) and <0.5 m/s if the slow metal vacancy mechanism dominates (Demouchy and Mackwell, 2006). Taken at face value, the results from the fast redox mechanism are more compatible with the embayment results determined here. It is worth noting that H^+ diffusion by the redox mechanism in olivine is on the same order of magnitude as H_2O diffusion in andesitic melt, which raises the question whether any H_2O-loss occurred through the olivine instead of exclusively through the melt in the embayment. However, diffusive equilibration through the olivine is also a function of its partition coefficient (Qin et al., 1992), which is very low in olivine ($Kd_{H2O}^{ol/liq} = 0.001$; Aubaud et al., 2004; Koga et al., 2003), and so equilibration will be much more efficient through the melt embayment to the bubble. Moreover, significant diffusive equilibration (>10%) was only observed for relatively small melt inclusions in the Fuego samples (<30 μm radius; Lloyd et al., 2013); the larger relative volume of the melt embayments (equivalent to a 100–200 μm diameter inclusion) would only experience 1–2% equilibration through the olivine over 10–30 min, based on the calculations in Lloyd et al. (2013, their Fig. 11).

A recent study has revealed a bimodal distribution of bubble sizes in eruptive products from the October 14 eruptive phase of 1974 Fuego eruption (Genareau et al., 2013). Bimodal distributions of bubble sizes and variations in the complexity of bubble shape have generally been thought to represent separate nucleation events during explosive eruptions (Blower et al., 2002). In the case of the October 14 phase, it was observed that the distribution of bubbles could be separated into two modes: one mode that was characterized by large but relatively rare bubbles and a second mode with small but very numerous bubbles. These two bubble modes have been interpreted to represent two vesiculation events that occur at a relatively greater depth (large mode) followed by a second event (small mode) at a later stage of ascent (Genareau et al., 2013). Without pressure estimates for this transition in nucleation style, we cannot thoroughly apply this to our model; however, these observations do lend support to multiple stages of decompression during magma ascent.

The 1974 eruption has been described as sub-Plinian with characteristics similar to some vulcanian eruptions (Rose et al., 1978). The 10-day eruption was characterized by explosions with a one-minute periodicity during each of the four main phases. All the samples studied here were collected on the same day and reflect volcanic material erupted in a 48-hour period; however, it is unlikely that all of these samples were erupted during the same explosion. Because there is a natural variability in the degree of explosivity during a given phase of the eruption, it is not likely that the decompression rate was constant over the course of the eruption, or even a single day. Based on this evidence, it should not be an expectation that all four embayments exhibit uniform decompression rates. Nonetheless, the relatively uniform decompression rates calculated (0.3–0.5 MPa/s in the upper ~7 km of the conduit) suggest that the embayment-hosting clasts experienced similar conditions during that phase of the eruption.

5.9. Comparison to previous embayment studies

Here we consider how our results compare to ascent rates calculated from previous embayment studies. For simplicity, we focus on the results of the single-stage model, which is well determined from H_2O and agrees with the faster stage of the two-stage model. The range of decompression rates calculated for the four embayments (0.32–0.47 MPa/s) represents the best fits, but here we also take into account the error associated with the NanoSIMS measurements. If we calculate best fit decompression rates for each embayment (Fig. 12), taking the minimum RMS ± 0.08 wt.% (1 SD at the maximum H_2O of 2.8 wt.% measured in the embayments), we find a range for all embayments of 0.24–0.60 MPa/s or ~8–21 m/s (Table 3a).

The embayment re-equilibration technique has been previously applied to two other explosive eruptions. Liu et al. (2007) measured concentration gradients in quartz-hosted melt pockets from the 26.5 ka Oruanui eruption of Taupo volcano, New Zealand and found that the results were best fit by a decompression rate of 0.001–0.007 MPa/s (0.04–0.35 m/s). The Oruanui eruption produced about 530 km^3 of moderate- to high-silica rhyolite magma (Wilson, 2001), which was relatively volatile rich (H_2O = 5.00 wt.%, CO_2 = 300 ppm). It is considered to be the largest volcanic eruption in the last 70 k years and was estimated to have had a volcanic explosivity index (VEI) of 8. In comparison to the decompression rates calculated for Fuego (Fig. 12), Oruanui is more than two orders of magnitude slower for an eruption that produced more than 5000 times the dense rock equivalent of the entire 1974 eruption of Fuego (>0.1 km^3, Rose et al., 1978). This calculation has been previously noted to be unusually slow for what is predicted from theoretical models (Papale et al., 1998; Rutherford, 2008), possibly a result of the large FTIR beam size that did not sample the minimum concentrations near the embayment outlet. This is an unexpected disparity because magma ascent rate has been suggested to scale with explosivity (Cashman, 2004); however, the eruptive complexities
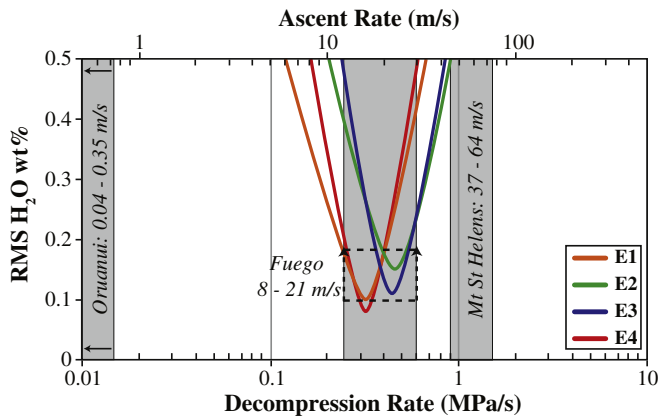
Fig. 12. Single-stage decompression rate results for Fuego embayments relative to previous embayment studies (Oruanui — Liu et al., 2007; Mt St Helens — Humphreys et al., 2008). Fuego embayment solutions are plotted against the RMS misfit for the model. The dashed box represents 2 RSD from an RMS value of 0.1 wt.% H_2O. This results in a range of decompression rates from 0.24 to 0.60 MPa/s (equivalent to 8–21 m/s) that satisfy the conditions for all four embayments. This exercise demonstrates that the solutions calculated for Fuego are unique relative to the two previous studies. Ascent rate on the top axis is applicable to the Fuego system only, and calculated using Eq. (5) in the text (Humphreys et al., 2008). For the other studies, gray bars represent the range of calculated decompression rates only.

associated with a catastrophic, caldera collapse may prevent a simple comparison with a standard sub-Plinian arc volcano such as Fuego.

Humphreys et al. (2008) analyzed plagioclase-hosted embayments and estimated a decompression rate for the plinian phase of the 1980 Mt. St. Helens (MSH) eruption ranging from 0.9 to 1.6 MPa/s (37–64 m/s), about half an order of magnitude faster than what we report for Fuego (Fig. 12). With a mass eruption rate about 1 order of magnitude greater than the October 14 phase of the Fuego eruption (1.44×10^7 kg/s), it appears that this is a case where magma ascent rate does scale with explosivity. However, there are a few differences in the methods and assumptions that preclude a direct comparison between the Fuego and MSH embayments. As was shown earlier, H_2O concentration profiles are most useful when analyzing the later stages of ascent (Fig. 6). Without the constraints from CO_2, S and major-element measurements, the initial conditions and the earliest stages of decompression at MSH are relatively less understood, potentially resulting in faster timescales. Additionally, it was assumed that the MSH magmatic system underwent an instantaneous pressure decrease from P_0 to P_F (230–30 MPa). For Fuego, the decompression model was systematically stepped through a closed-system degassing path, which we assumed was more appropriate for this sub-Plinian eruption. This results in a smaller concentration gradient throughout the majority of the diffusion model for Fuego, resulting in longer time scales.

The MSH and Fuego embayments also differ in terms of the lowest measured H_2O concentrations. Whereas we measure concentrations as low as 0.76 wt.% in the embayments (Table 2) and 0.04 wt.% in the matrix glass, Humphreys et al. assumed H_2O_F concentrations between 1.0 and 2.0 wt.%, which minimizes the pressure drop and effectively reduces the overall time required for re-equilibration. The elevated H_2O concentrations at the outlet for the MSH embayments and in the matrix glass were interpreted as evidence for disequilibrium degassing. Given the potential for supersaturation of H_2O in rhyolitic systems at decompression rates >0.25 MPa/s (Gardner et al., 1999), Humphreys et al. suggested that the reported decompression rates were potentially overestimated as a result of assuming equilibrium degassing. The fast decompression rates estimated for the Fuego embayments introduce the possibility of disequilibrium degassing for the Fuego magmatic system as well. Given the greater D_{H_2O} in mafic melt and the similarity of the lowest measured concentrations of H_2O in the embayments with the measured groundmass concentrations (Fig. 3), the extent of super-saturation and disequilibrium degassing of H_2O during decompression

may be limited in the Fuego magmatic system. Although H_2O may be undergoing equilibrium degassing, CO_2-over-saturated basaltic melts have been generated experimentally for ascent rates greater than ~1.5 m/s (Pichavant et al., 2013). However, Fuego MIs show no obvious signs of disequilibrium degassing, which would manifest as CO_2 in excess of closed system degassing. Instead, closed-system degassing is an adequate model for H_2O–CO_2 and S (Fig. 5), and the inferred vapor/liquid partition coefficients for S are consistent with equilibrium values (Fiege et al., 2014) at an fO_2 near QFM + 1 (as for Fuego, Lloyd et al., 2013). Because S has a lower diffusivity than CO_2, we likewise expect CO_2 to reflect near equilibrium degassing at Fuego. Finally, the success in fitting both H_2O and S diffusion profiles with the same decompression rate supports the equilibrium degassing model we use.

Direct comparison of embayment-derived ascent velocities for the different eruptions (e.g., Oranui, Mt St Helens and Fuego) is complicated by the different magma viscosities and degassing styles. Future research in diffusion chronometry, especially on similar volcanic systems that exhibit varying explosive styles, is necessary to reveal further insights into magma ascent during explosive volcanism.

6. Conclusions

We have analyzed four olivine-hosted embayments erupted on October 17, 1974 at Volcán de Fuego for the purpose of assessing magma ascent velocities during explosive basaltic eruptions. Utilizing a NanoSIMS to measure multi-volatile profiles, we observed that H_2O, CO_2, and S decrease in concentration toward outlet bubbles, consistent with decreasing diffusive loss. Cl and F vary little in concentration throughout the embayment, consistent with their lack of degassing over most of the ascent path. We also observe sharp gradients in major-element concentrations in the outer 20–40 μm of the embayment that could be produced by crystallization at the bubble/melt boundary. Because D_{H_2O} is compositionally dependent, a parameterization was designed specifically to account for the effects of this chemical boundary layer on diffusivities. We defined the initial and external melt conditions for the decompression model based on the closed-system degassing path defined by the MI population. A numerical diffusion model is used to fit the compositional profiles along the embayments, with continuously varying diffusivities and external melt compositions as a function of pressure. The primary control on the length scale and shape of the concentration profiles is the decompression rate.

We present two scenarios for the decompression of the Fuego magma prior to eruption. One scenario assumes a constant decompression rate throughout ascent. In this case, the free variables are constrained in the following order: P_0 is established by the inferred initial sulfur that is allowed to vary between the four embayments; P_F is set by an extrapolation from the measurements closest to the bubble and is constant for all embayments; and dP/dt was found for each embayment by fitting to the measured H_2O profile. This method resulted in decompression rates ranging from 0.32 to 0.47 MPa/s (11.0–16.5 m/s), which notably also fit the sulfur profiles, except for those without monotonic shapes. The CO_2 profiles could only be fit in the constant decompression models by adjusting the initial CO_2 concentrations independently of the other volatiles. Better fits were also obtained for CO_2 using a two-stage model: an initial slow stage followed by a faster second stage. Decompression rates calculated with this method ranged from 0.05 to 0.28 MPa/s and 0.32 to 0.47 MPa/s for the first and second stages respectively, and may record the acceleration of the magma during ascent. The slower, first stage is not well constrained, and could occur over minutes to hours. The second stage rates are very similar to the constant decompression model, as both are primarily sensitive to H_2O degassing at pressures lower than 145 MPa.

For this reason we define the minimum and maximum decompression rates calculated for this eruption based on the constant decompression results, which range from 0.24 to 0.60 MPa/s (~8–21 m/s) for all four embayments when taking into account analytical uncertainties.

Within the context of the October 17 eruption at Fuego, the ascent rates calculated in this study compare favorably to estimates based on mass eruption rate and prior MI re-equilibration timescales. The calculated decompression rates also fall within a fairly limited range that is consistent with the explosivity of this sub-Plinian eruption. These results should encourage the further use of embayments to constrain magma ascent dynamics for a wider range of magma types and eruptive styles.

Acknowledgments

Appendix A. Supplementary data

Supplementary data to this article can be found online at http://dx.doi.org/10.1016/j.jvolgeores.2014.06.002.

References

Anderson Jr., A.T., 1991. Hourglass inclusions: theory and application to the Bishop Rhyolitic Tuff. Am. Mineral. 76, 530–547.

Aubaud, C., Hauri, E.H., Hirschmann, M.M., 2004. Hydrogen partition coefficients between nominally anhydrous minerals and basaltic melts. Geophys. Res. Lett. 31, L20611.

Baker, D.R., Freda, C., Brooker, R.A., Scarlato, P., 2005. Volatile diffusion in silicate melts and its effects on melt inclusions. Ann. Geophys. 48, 699–717.

Behrens, H., Stelling, J., 2011. Diffusion and redox reactions of sulfur in silicate melts. Rev. Mineral. Geochem. 73, 79–111.

Behrens, H., Zhang, Y., Xu, Z., 2004. H_2O diffusion in dacitic and andesitic melts. Geochim. Cosmochim. Acta 68, 5139–5150.

Berlo, K., Stix, J., Roggensack, K., Ghaleb, B., 2012. A tale of two magmas, Fuego, Guatemala. Bull. Volcanol. 74, 377–390.

Blower, J.D., Keating, J.P., Mader, H.M., Phillips, B., 2002. The evolution of bubble size distributions in volcanic eruptions. J. Volcanol. Geotherm. Res. 120, 1–23.

Blundy, J.D., Cashman, K.V., Rust, A.C., Witham, F., 2010. A case for CO_2-rich arc magmas. Earth Planet. Sci. Lett. 290, 289–301.

Carr, M.J., Walker, J.A., 1987. Intra-eruption changes in composition of some mafic to intermediate tephras in Central-America. J. Volcanol. Geotherm. Res. 33, 147–159.

Cashman, K.V., 2004. Volatile controls on magma ascent and degassing. AGU Monogr. 150, 109–124.

Cashman, K.V., Sparks, R.S.J., 2013. How volcanoes work: a 25 year perspective. Geol. Soc. Am. Bull. 125, 664–690.

Castro, J.M., Dingwell, D.B., 2009. Rapid ascent of rhyolitic magma at Chaitén volcano, Chile. Nature 461, 780–783.

Chen, Y., Provost, A., Schiano, P., Cluzel, N., 2013. Magma ascent rate and initial water concentration inferred from diffusive water loss from olivine-hosted melt inclusions. Contrib. Mineral. Petrol. 165, 525–541.

Costa, F., Morgan, D., 2010. Time constraints from chemical equilibration in magmatic crystals. In: Dosseto, A., Turner, S., Van Orman, J.A. (Eds.), Timescales of Magmatic Processes: From Core to Atmosphere. Wiley-Blackwell, pp. 125–159.

Demouchy, S., Mackwell, S.J., 2006. Mechanisms of hydrogen incorporation and diffusion in iron-bearing olivine. Phys. Chem. Miner. 33, 347–355.

Demouchy, S., Jacobsen, S.D., Gaillard, F., Stern, C.R., 2006. Rapid magma ascent recorded by water diffusion profiles in mantle olivine. Geology 34, 429–432.

Endo, E.T., Murray, T.L., Power, J.A., 1996. A comparison of pre-eruption, real-time seismic amplitude measurements for eruptions at Mount St. Helens, Redoubt Volcano, Mount Spurr, and Mount Pinatubo. In: Newhall, C.G., Punongbayan, R.S. (Eds.), Fire & Mud: Eruptions and Lahars of Mount Pinatubo, Philippines. University of Washington Press, pp. 233–246.

Farver, J.R., 2010. Oxygen and hydrogen diffusion in minerals. Rev. Mineral. Geochem. 72, 447–507.

Faure, F., Schiano, P., 2005. Experimental investigation of equilibration conditions during forsterite growth and melt inclusion formation. Earth Planet. Sci. Lett. 236, 882–898.

Fiege, A., Behrens, H., Holtz, F., Adams, F., 2014. Kinetic vs. thermodynamic control of degassing of $H_2O–S \pm Cl$-bearing andesitic melts. Geochim. Cosmochim. Acta 125, 241–264.

Gardner, J.E., Hilton, M., Carroll, M.R., 1999. Experimental constraints on degassing of magma: isothermal bubble growth during continuous decompression from high pressure. Earth Planet. Sci. Lett. 168, 201–218.

Genareau, M.J., Mulukutlu, G.K., Proussevitch, A.A., Durant, A.J., Rose, W.I., Sahagian, D.L., 2013. The size range of bubbles that produce ash during explosive volcanic eruptions. J. Appl. Volcanol. 2, 4. http://dx.doi.org/10.1186/2191-5040-2-4.

Geschwind, C.H., Rutherford, M.J., 1995. Crystallization of microlites during magma ascent: the fluid mechanics of 1980–86 eruptions at Mount St. Helens. Bull. Volcanol. 57, 356–370.

Gonnermann, H.M., Manga, M., 2007. The fluid mechanics of volcanic eruptions. Annu. Rev. Fluid Mech. 39, 321–356.

Gudmundsson, M.T., Thordarson, T., Höskuldsson, A., Larsen, G., Björnsson, H., Prata, F.J., Oddsson, B., Magnússon, E., Högnadóttir, T., Petersen, G.N., Hayward, C.L., Stevenson, J.A., Jónsdóttir, I., 2012. Ash generation and distribution from the April–May 2010 eruption of Eyjafjallajokull, Iceland. Sci. Rep. 2, 572. http://dx.doi.org/10.1038/srep00572.

Hauri, E.H., Shaw, A.M., Wang, J., Dixon, J.E., King, P.L., Mandeville, C., 2006. Matrix effects in hydrogen isotope analysis of silicate glasses by SIMS. Chem. Geol. 235, 352–365.

Hauri, E.H., Weinreich, T., Saal, A.E., Rutherford, M.C., Van Orman, J.A., 2011. High pre-eruptive water contents preserved in lunar melt inclusions. Science 333, 213–215.

Humphreys, M.C.S., Menand, T., Blundy, J.D., Klimm, K., 2008. Magma ascent rates in explosive eruptions: constraints from H_2O diffusion in melt inclusions. Earth Planet. Sci. Lett. 270, 25–40.

Kelley, K.A., Cottrell, E., 2012. The influence of magmatic differentiation on the oxidation state of Fe in a basaltic arc magma. Earth Planet. Sci. Lett. 329–330, 109–121.

Koga, K., Hauri, E.H., Hirschmann, M., Bell, D., 2003. Hydrogen concentration analyses using SIMS and FTIR: comparison and calibration for nominally anhydrous minerals. Geochem. Geophys. Geosyst. 4. http://dx.doi.org/10.1029/2002GC000378.

Kohlstedt, D.L., Mackwell, S.J., 1998. Diffusion of hydrogen and intrinsic point defects in olivine. Z. Phys. Chem. 207, 147–162.

Lange, R.A., Carmichael, I.S.E., 1987. Densities of $Na_2O–K_2O–CaO–MgO–FeO–Fe_2O_3–Al_2O_3–TiO_2–SiO_2$ liquids: new measurements and derived partial molar properties. Geochim. Cosmochim. Acta 51, 2931–2946.

Lesne, P., Kohn, S., Blundy, J., Witham, F., Botcharnikov, R., Behrens, H., 2011. Experimental simulation of closed-system degassing in the system basalt–$H_2O–CO_2–S–Cl$. J. Petrol. 52, 1737–1762.

Liu, Y., Anderson, A.T., Wilson, C.J.N., 2007. Melt pockets in phenocrysts and decompression rates of silicic magmas before fragmentation. J. Geophys. Res. 112, B06204. http://dx.doi.org/10.1029/2006JB004500.

Lloyd, A.S., Plank, T., Ruprecht, P., Hauri, E.H., Rose, W., 2013. Volatile loss from melt inclusions in pyroclasts of differing sizes. Contrib. Mineral. Petrol. 165, 129–153.

Mastin, L.G., Ghiorso, M.S., 2000. A numerical program for steady-state flow of magma–gas mixtures through vertical eruptive conduits. U.S. Geol. Surv. Open-File Rep. 00–209.

Metrich, N., Wallace, P.J., 2008. Volatile abundances in basaltic magmas and their degassing paths tracked by melt inclusions. Rev. Mineral. Geochem. 69, 273–331.

Mysen, B.O., Richet, P., 2005. Silicate Glasses and Melts: Properties and Structure. Elsevier Science.

Newman, S., Lowenstern, J.B., 2002. Volatile-calc: a silicate melt–$H_2O–CO_2$ solution model written in Visual Basic for Excel. Comput. Geosci. 28, 597–604.

Ni, H., Xu, Z., Zhang, Y., 2013. Hydroxyl and molecular H_2O diffusivity in haploandesitic melt. Geochim. Cosmochim. Acta 103, 36–48.

Nowak, M., Schreen, D., Spickenbom, K., 2004. Argon and CO_2 on the race track in silicate melts: a tool for the development of a CO_2 speciation and diffusion model. Geochim. Cosmochim. Acta 68, 5127–5138.

Ochs, F.A., Lange, R.A., 1999. The density of hydrous magmatic liquids. Science 283, 314–317.

Okumura, S., Nakashima, S., 2006. Water diffusion in basaltic to dacitic glasses. Chem. Geol. 227, 70–82.

Papale, P., Neri, A., Macedonio, G., 1998. The role of magma composition and water content in explosive eruptions, 1. Conduit ascent dynamics. J. Volcanol. Geotherm. Res. 87, 75–93.

Persikov, E.S., Newman, S., Bukhtiyarov, P.G., Nekrasov, A.N., Stolper, E.M., 2010. Experimental study of water diffusion in haplobasaltic and haploandesitic melts. Chem. Geol. 276, 241–256.

Peslier, A.H., Luhr, J.F., 2006. Hydrogen loss from olivines in mantle xenoliths from Simcoe (USA) and Mexico: mafic alkalic magma ascent rates and water budget of the subcontinental lithosphere. Earth Planet. Sci. Lett. 242, 302–319.

Pichavant, M., Di Carlo, I., Rotolo, S.G., Scaillet, B., Burgisser, A., Le Gall, N., Martel, C., 2013. Generation of CO_2 rich melts during basalt magma ascent and degassing. Contrib. Mineral. Petrol. 166, 545–561.

Proussevitch, A., Sahagian, D.L., 2005. Bubbledrive-1: a numerical model of volcanic eruption mechanisms driven by disequilibrium magma degassing. J. Volcanol. Geotherm. Res. 143, 89–111.

Qin, Z., Lu, F., Anderson, A.T., 1992. Diffusive re-equilibration of melt and fluid inclusions. Am. Mineral. 77, 565–576.

Roggensack, K., 2001. Unraveling the 1974 eruption of Fuego volcano (Guatemala) with small crystals and their young melt inclusions. Geology 29, 911–914.

Rose, W.I., Anderson, A.T., Woodruff, L.G., Bonis, S.B., 1978. October 1974 basaltic tephra from Fuego Volcano — description and history of magma body. J. Volcanol. Geotherm. Res. 4, 3–53.

Rose, W.I., Self, S., Murrow, P.J., Bonadonna, C., Durant, A.J., Ernst, G.J., 2008. Nature and significance of small volume fall deposits at composite volcanoes: insights from the October 14, 1974 Fuego eruption, Guatemala. Bull. Volcanol. 70, 1043–1067.

Ruprecht, P., Plank, T., 2013. Feeding andesitic eruptions with a high-speed connection from the mantle. Nature 500, 68–72.

Rutherford, M.J., 2008. Magma ascent rates. Rev. Mineral. Geochem. 69, 241–271.

Rutherford, M.J., Devine, J.D., 2003. Magmatic conditions and magma ascent as indicated by hornblende phase equilibria and reactions in the 1995–2001 Soufriere Hills magma. J. Petrol. 44, 1433–1454.

Sisson, T.W., Layne, G.D., 1993. H$_2$O in basalt and basaltic andesite glass inclusions from 4 subduction related volcanoes. Earth Planet. Sci. Lett. 117, 619–635.

Spera, F.J., 1984. Carbon dioxide in petrogenesis III: role of volatiles in the ascent of alkaline magma with special reference to xenolith-bearing magmas. Contrib. Mineral. Petrol. 88, 217–232.

Szramek, L, Gardner, J.E., Larsen, J., 2006. Degassing and microlite crystallization of basaltic andesite magma erupting at Arenal volcano, Costa Rica. J. Volcanol. Geotherm. Res. 157, 182–201.

Toramaru, A., 2006. BND (bubble number density) decompression rate meter for explosive volcanic eruptions. J. Volcanol. Geotherm. Res. 154, 303–316.

Wilson, C.J.N., 2001. The 26.5 ka Oruanui eruption, New Zealand: an introduction and overview. J. Volcanol. Geotherm. Res. 112, 133–174.

Wilson, L, Sparks, R.S.J., Walker, G.P.L., 1980. Explosive volcanic eruptions — IV. The control of magma properties and conduit geometry on eruption column behavior. Geophys. J. Int. 63, 117–148.

Witham, F., Blundy, J., Kohn, S.C., Lesne, P., Dixon, J., Churakov, S.V., Botchamikov, R., 2012. SolEx: a model for mixed COHSCl-volatile solubilities and exsolved gas compositions in basalt. Comput. Geosci. http://dx.doi.org/10.1016/j.cageo.2011.09.021.

Zhang, Y., Cherniak, D.J., 2010. Diffusion in minerals and melts: introduction. Rev. Mineral. Geochem. 72, 1–4.

Zhang, Y., Ni, H., 2010. Diffusion of H, C, and O components in silicate melts. Rev. Mineral. Geochem. 72, 171–225.

Zhang, Y., Xu, Z., Zhu, M., Wang, H., 2007. Silicate melt properties and volcanic eruptions. Rev. Geophys. 45, RG4004. http://dx.doi.org/10.1029/2006RG000216.

Zhang, Y., Ni, H., Chen, Y., 2010. Diffusion data in silicate melts. Rev. Mineral. Geochem. 72, 311–408.